



Full Length Article

Synthesis of new non-covered and silica-covered $Y_{0.9}Tm_{0.1-x}Yb_xVO_4$ nanophosphors with emission in the visible and NIR ranges

Y. Lozano^a, J. Isasi^{a,**}, M. Fernández-Ramos^{a,b,*}, M. Rapp^a, M. Alcolea Palafox^b,
E. Ortiz-Rivero^c, T. Muñoz-Ortiz^c

^a Departamento de Química Inorgánica, Facultad de Ciencias Químicas, Universidad Complutense de Madrid, Ciudad Universitaria S/n, 28040, Madrid, Spain

^b Departamento de Química Física, Facultad de Ciencias Químicas, Universidad Complutense de Madrid, Ciudad Universitaria S/n, 28040, Madrid, Spain

^c Nanomaterials for Bioimaging Group (nanoBIG), Departamento de Física de Materiales, Facultad de Ciencias, Universidad Autónoma de Madrid, C/ Francisco Tomás y Valiente 7, 28049, Madrid, Spain

ARTICLE INFO

Keywords:

Nanophosphors
Sol-gel chemistry
Hydrothermal synthesis
Luminescence studies

ABSTRACT

The development of new materials of interest in the bioimaging field is a relevant topic in current research. We present and study here novel non-covered and silica-covered $Y_{0.9}Tm_{0.1-x}Yb_xVO_4$ samples with $x = 0, 0.01, 0.05$ and 0.09 that were prepared by hydrothermal synthesis. For comparison purposes, the study of $Y_{0.9}Tm_{0.1}VO_4$ sample synthesized by the sol-gel method was also included. The relationships between the synthesis method, dopant content and luminescence emission were systematically studied by X-ray diffraction (XRD), FTIR spectroscopy and transmission electron microscopy (TEM). XRD profiles and FTIR spectra confirm the zircon-type structure of the obtained samples. Particles of two different morphologies were found in TEM images of uncoated samples, some spherical with sizes between 42 and 50 nm and others elongated. A shell thickness between 8 and 13 nm was also observed in silica-covered samples. Photoluminescence studies of our samples revealed emission in the NIR and visible ranges. Under excitation at 790 nm, the spectra of thulium-doped samples showed the characteristic emission band of Tm^{3+} ions. Substitution of thulium by ytterbium successfully led to an up-conversion emission under excitation at 980 nm. Finally, the fluorescent emission study in the NIR of samples that could be more biocompatible demonstrated that they are suitable for use as luminescent thermometers in the physiological temperature range.

1. Introduction

Lanthanide ion (Ln^{3+}) activated phosphors are light-emitting materials consisting of a host lattice doped with a small amount of Ln^{3+} ions. These materials have been attracting the interest of the scientific community lately due to their physical and chemical stability, high luminescence intensity, long useful lifetime, and wide range of emission colours [1,2]. All these characteristics make them ideal for their use as fluorescent sensors or in the design of both optoelectronic and imaging devices, the latter being useful in biomedicine [3–10]. When studying the luminescence of any Ln^{3+} activated phosphor material, it is found that their luminescent emission depends on: (i) the specific host lattice in which they crystallize, the type and concentration of dopant lanthanide ions, the environment of these sensitizing ions and/or

luminescence activators in the host lattice [11]; and (ii) the size, shape and organization of the particles of that material sample [12,13], since the particle size affects the luminescent intensity.

Choosing the ideal lattice is a key factor when preparing samples of Ln^{3+} ion activated phosphors. Suitable host lattices should present low phonon energy and high radiative transitions, while the hosted lanthanide ions should also have high emission efficiency and a controlled emission profile within a crystallographic environment of high chemical stability [14]. The latter is due to the considerably influence of the environment of the nearest neighbouring atoms on the luminescent emission of these host ions. In fact, an increase in covalence causes a decrease in the interaction between electrons, resulting in electronic transitions at lower energy [15,16].

The crystallographic environment around the host cation determines

* Corresponding author. Departamento de Química Inorgánica, Facultad de Ciencias Químicas, Universidad Complutense de Madrid, Ciudad Universitaria S/n, 28040, Madrid, Spain.

** Corresponding author.

E-mail addresses: isasi@ucm.es (J. Isasi), migufe04@ucm.es (M. Fernández-Ramos).

<https://doi.org/10.1016/j.jlumin.2023.119708>

Received 2 June 2022; Received in revised form 31 December 2022; Accepted 13 January 2023

Available online 20 January 2023

0022-2313/© 2023 The Authors. Published by Elsevier B.V. This is an open access article under the CC BY-NC-ND license (<http://creativecommons.org/licenses/by-nc-nd/4.0/>).

the symmetry of their electrostatic interaction since the magnitude of the interaction energy of the crystal field depends both on the distance between the nearest neighbours and on the covalent character of the bonds [12]. However, the emission of lanthanide ions activated phosphors shows that the spectral position is rarely affected by its chemical surrounding because of the shielding of the Ln^{3+} 4f electrons by the outer $5s^2$ and $5p^6$ shells. Thus, the f-f transitions are not influenced by external crystal fields, leading to very sharp fluorescent emission bands corresponding to intra 4f-4f or 4f-5d electronic transitions [12,15]. The intensity of these emissions between different J -number levels depends on the symmetry of the local environment of Ln^{3+} and it can be described in terms of the Judd–Ofelt theory [17–19]. The fluorescent emission lines of lanthanide ions in lanthanide ion activated phosphors samples are caused by electric dipole (ED) and magnetic dipole (MD) transitions, the former being very sensitive to site symmetry, while the latter is not influenced by the environment symmetry [20–22]. According to the Judd–Ofelt theory [17–19], MD type transitions are allowed, while ED transitions are forbidden and only occur when the lanthanide ions occupy a position in the lattice without a symmetry center. For this reason, direct excitation of lanthanide ions is a rather inefficient process, although this feature can be solved by placing lanthanides in host lattices showing positions with low symmetry [23–25]. Regardless of how the excited states of Ln^{3+} are populated, the decay mechanism is the same for most of the Ln^{3+} ion activated phosphors. Generally, these materials originate down-shift processes, but also up-conversion (UC) processes, a successful method of generating visible light by photo-excitation at a longer wavelength [26–29]. In down-shifting samples, the inorganic host lattice acts not only as a host crystal for the Ln^{3+} ions, but also as a sensitizer of their luminescence. However, despite the single Ln^{3+} doping model, it is also possible to co-dope with two ions: one acting as an activator (light-emitting center), and another as a sensitizer with a higher absorption coefficient. This approach generally provides much more efficient luminescence emission by taking advantage of the energy transfer (ET) process from the sensitizer to the activators [30].

In UC materials, it is important that the optical properties of the sensitizers and the emitting ions match each other very well [31–33]. Therefore, the focus lies on the UC process and the photoexcitation wavelength in the near infrared (NIR). The use of lower-energy photo-excitation is associated with significant advantages, such as negligible photodamage, low autofluorescence background, and higher penetration into biological tissues [34–36]. Ytterbium ions are used as excellent luminescence sensitizers for other lanthanide ions due to their effective absorption cross-section at 980 nm. In fact, the thulium/ytterbium ($\text{Tm}^{3+}/\text{Yb}^{3+}$) pair has been studied in different nanocrystals, glasses, or glass-ceramics to improve the spectroscopic properties of the materials [15,30,37]. Recent publications on UC and down conversion studies (DC) have also described the benefits of using erbium/ytterbium ($\text{Er}^{3+}/\text{Yb}^{3+}$) doped nanoparticles as nanothermometers and nano-heaters, as well as for *in-vivo* applications in bioimaging [12,38,39]. Therefore, fluorescent nanothermometers are being widely studied in thermometry due to their high spatial resolution, remote sensing, and fast response, which is displayed in the good temperature-dependence of their emission intensity [40]. Temperature measurements are usually analysed using the fluorescence intensity ratio (FIR), which is an integral ratio of the thermally coupled energy levels of Ln^{3+} ions with a typical energy difference between 200 and 2000 cm^{-1} [41].

As indicated above, the luminescent emission of Ln^{3+} activated phosphors also depend on the morphology of the powder samples to be studied. Therefore, it is evident that improvements in luminescence features require the selection of well-defined synthesis methods. The synthesis of these compounds has been widely studied using different soft chemistry routes [42–44], including the hydrothermal or solvothermal synthesis [38,45–47], chemical coprecipitation [48–50], microemulsion [51,52] and sol-gel methods [45–47,53]. These routes provide a controlled synthesis in which the different reaction parameters

(type of solvent, concentration, additive, temperature, and reaction time) can be varied in a controlled way to obtain material samples with the desired properties. With soft chemical routes, it is also possible to include simple and straightforward steps to cover the surface of samples with ligands, thus avoiding particle aggregation when dispersed in an aqueous or organic media [45,54,55].

Nanoparticles have a large surface/volume ratio, which results in more surface defects per unit volume in samples obtained at nanometer size. Surface defects increase the non-radiative decay and quenching effect (due to high-energy vibrations of surface-associated solvents and ligands), which reduces the luminescent emission intensity. To avoid this feature, silica has been used as coating and it has been found that the inert shell reduces the luminescence quenching effects [12,38,56,57]. The most common ways to obtain silica-coated UC nanoparticles are by the Stöber method or by microemulsion synthesis [58–60]. Silica shows important advantages for these purposes since it is chemically inert, biocompatible and shows optical transparency in the visible and NIR ranges [12,38,61–64]. NIR light excitation allows deep penetration into biological tissue with little damage and provides low background signals by avoiding autofluorescence from unexcited biological media [65].

In addition to surface defects, it is known that many of the discrete energy levels of the activator ions are also sensitive to the luminescence quenching effects as dopant concentration increases [66]. All these reasons indicate that the study of new luminescent samples with different compositions and silica coatings is required to obtain materials with high luminescent emission intensity.

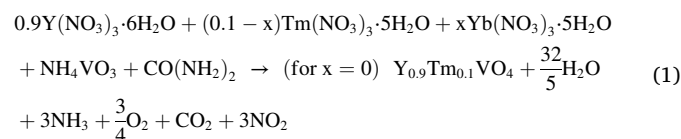
On this basis, the obtaining and study of new uncoated and silica-coated $\text{Y}_{0.9}\text{Tm}_{0.1-x}\text{Yb}_x\text{VO}_4$ samples with $x = 0, 0.01, 0.05, 0.09$ is described here. A sample with $x = 0$ was prepared both by hydrothermal synthesis with urea addition and by sol-gel method. The remaining samples were only prepared by hydrothermal synthesis. The relationships between the synthesis method, dopant content and luminescence emission were systematically studied by XRD, FTIR spectroscopy and TEM. Emission spectra of these samples in the NIR and visible ranges and their potential use as luminescent thermometers in the physiological temperature range were also investigated.

2. Materials and methods

$\text{Y}_{0.9}\text{Tm}_{0.1-x}\text{Yb}_x\text{VO}_4$ samples with $x = 0, 0.01, 0.05$ and 0.09 were prepared by hydrothermal synthesis with urea addition and, for a comparative study, the sample with $x = 0$ was also prepared by the sol gel method. Yttrium, thulium and ytterbium nitrates $\text{Y}(\text{NO}_3)_3 \cdot 6\text{H}_2\text{O}$ (99.8%, Strem Chemicals), $\text{Tm}(\text{NO}_3)_3 \cdot 5\text{H}_2\text{O}$ (99.9%, Strem Chemicals), $\text{Yb}(\text{NO}_3)_3 \cdot 5\text{H}_2\text{O}$ (99.9% Sigma-Aldrich) as well as ammonium vanadate NH_4VO_3 ($\geq 99\%$, Sigma Aldrich analytical grade) were used as starting precursors. In addition, urea ($\text{CO}(\text{NH}_2)_2$) (PanReac, 99.0–100.5%), citric acid ($\text{C}_6\text{H}_8\text{O}_7$, CA) ($\geq 99\%$, Sigma Aldrich) and ethylene glycol ($\text{C}_2\text{H}_6\text{O}_2$, EG) (99%, PanReac) were used as dispersing, complexing, and polymerizing agents, respectively.

2.1. Hydrothermal synthesis

The hydrothermal synthesis of $\text{Y}_{0.9}\text{Tm}_{0.1-x}\text{Yb}_x\text{VO}_4$ samples with $x = 0, 0.01, 0.05$ and 0.09 was carried out from the precursors described previously. Stoichiometric amounts of the corresponding precursors, calculated according to reaction (1), were placed into a beaker and dissolved in 100 mL of deionized water.



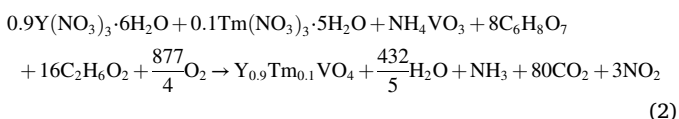
All solutions were heated at 100 °C and stirred for 60 min. In all cases, urea was added because it is a good dispersing agent that allowed

the formation of a stable suspension and prevented the agglomeration of nanoparticles in the reaction medium [67]. Later, the pH value was adjusted to 10 with the addition of NH_3 25%. This reaction medium favours the production of nanoparticles with higher intensity of luminescent emission [45]. These solutions were kept under heating and magnetic stirring for an additional hour and then were aged for 5 days to promote nanoparticle formation.

The resulting mixtures were placed in Teflon-lined stainless-steel autoclaves where they were heated at 220°C for 6 h. Then, the obtained powders were dried at low temperature ($50\text{--}80^\circ\text{C}$) to avoid the growth of the particles. Finally, yellowish powder samples were obtained which were named as $\text{Y}_{0.9}\text{Tm}_{0.1-x}\text{Yb}_x\text{VO}_4$ -HT. Scheme of the preparation process is shown in Fig. 1.

2.2. Sol-gel synthesis

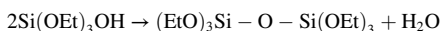
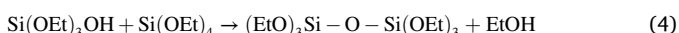
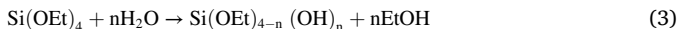
To obtain $\text{Y}_{0.9}\text{Tm}_{0.1}\text{VO}_4$ sample, the stoichiometric amounts of the precursors were calculated according to reaction (2).



0.25 g of NH_4VO_3 and the corresponding stoichiometric quantities of $\text{Y}(\text{NO}_3)_3 \cdot 6\text{H}_2\text{O}$ and $\text{Tm}(\text{NO}_3)_3 \cdot 5\text{H}_2\text{O}$ were dissolved in a beaker by adding 100 mL of deionized water. This solution was heated to 100°C , being subjected to magnetic stirring for 30 min. Then, CA was added in a ratio 8:1 with respect to the amount of ammonium vanadate [12]. This medium favours the reaction by improving the crystallinity of the phase obtained [45]. After that, EG was added in a 16:1 M ratio, which acts as a polymeric agent to improve weak interactions between the particles formed during crystallization [12]. The gel obtained was aged for 4 days and dried at 200°C to obtain a black powder that was subsequently heated at 450°C for 6 h to get a final white-colour sample, which was labelled as $\text{Y}_{0.9}\text{Tm}_{0.1}\text{VO}_4$ -SG. The synthesis process is shown in Fig. 2.

2.3. Silica coating tests of $\text{Y}_{0.9}\text{Tm}_{0.1-x}\text{Yb}_x\text{VO}_4$ samples with $x = 0, 0.01, 0.05$ and 0.09

Silica coated samples were prepared using the Stöber method [68]. This method involves hydrolysis (3) and condensation (4) processes:



0.1 g of $\text{Y}_{0.9}\text{Tm}_{0.1}\text{VO}_4$ -HT, $\text{Y}_{0.9}\text{Tm}_{0.1}\text{VO}_4$ -SG and $\text{Y}_{0.9}\text{Tm}_{0.1-x}\text{Yb}_x\text{VO}_4$ -HT samples with $x = 0.01, 0.05$ and 0.09 were dissolved in 50 mL of deionized water and 15 mL of ethanol. Resulting solutions were sonicated for 15 min to achieve homogenized suspensions and then, under magnetic stirring and heating, 10 mL of NH_3 25% were added. Finally, 2 mL of TEOS (Merck) were added dropwise to each of these solutions during 3 h. The obtained

powders were separated by centrifugation and dried at 75°C for 12 h. Final samples were named $\text{Y}_{0.9}\text{Tm}_{0.1}\text{VO}_4$ -HT@ SiO_2 , $\text{Y}_{0.9}\text{Tm}_{0.1}\text{VO}_4$ -SG@ SiO_2 and $\text{Y}_{0.9}\text{Tm}_{0.1-x}\text{Yb}_x\text{VO}_4$ -HT@ SiO_2 .

2.4. Characterization techniques

A full structural characterization of non-covered and silica-covered $\text{Y}_{0.9}\text{Tm}_{0.1-x}\text{Yb}_x\text{VO}_4$ samples with $x = 0, 0.01, 0.05$ and 0.09 has been carried out by X-ray diffraction (XRD) and Fourier transform infrared (FTIR) spectra.

XRD patterns of the synthesized samples were recorded on a PANalytical XPERT-PRO diffractometer using $\text{Cu K}\alpha$ radiation, with a step length of 0.04° and a step time of 1 s. The instrumental broadening of the observed reflections was considered and calibrated by using the LaB_6 standard NIST SRM 660 b. From XRD patterns, an estimation of the average crystalline size (D) was also carried out using the Scherrer equation [69].

$$D = \frac{K\lambda}{\beta \cdot \cos \theta} \quad (5)$$

In this equation, λ is the wavelength of X-ray radiation (1.54186 \AA), K is a dimensionless form factor with a value of 0.89 if spherical particles are considered, β is the full width at half maximum (FWHM) of the diffraction peaks and θ is the diffraction angle.

FTIR spectra were recorded using a PerkinElmer FTIR spectrometer and pressing the powder against a diamond tip. Measurements were carried out in the $400\text{--}4000 \text{ cm}^{-1}$ range and with a resolution of 4 cm^{-1} .

The powder morphology of the synthesized samples was determined by transmission electron microscopy (TEM) images, which were obtained in a JEOL 2100 F transmission electron microscope operating at 200 kV and equipped with a field emission electron gun that provides a point resolution of 0.19 nm. To obtain the images, the samples were dispersed in *n*-butanol and the drops of the corresponding suspensions were deposited on carbon-coated copper grids.

The absorption spectra of the samples were measured using a PerkinElmer Lambda 950 UV/Vis spectrometer, which can operate in the $175\text{--}3300 \text{ nm}$ range. These samples were measured in powder form and the spectrum was recorded in the selected range of $600\text{--}1700 \text{ nm}$. The emission spectra in the NIR region ($900\text{--}1600 \text{ nm}$) of these samples were recorded by excitation with a continuous diode laser at 790 nm and a Synapse Horiba Jobin Yvon detector. To obtain the up-conversion spectra of these samples, they were excited with a diode laser at 980 nm.

3. Results and discussion

3.1. X-ray diffraction studies

XRD patterns of $\text{Y}_{0.9}\text{Tm}_{0.1}\text{VO}_4$ -SG and $\text{Y}_{0.9}\text{Tm}_{0.1}\text{VO}_4$ -HT samples are shown in Fig. 3. As can be seen, XRD pattern of $\text{Y}_{0.9}\text{Tm}_{0.1}\text{VO}_4$ -HT sample treated at 220°C shows that other phases are also present besides the YVO_4 oxide. These phases are the following oxides: Y_2O_3 [JCPDS file card no. 01-083-0927] and V_2O_5 [JCPDS file card no. 01-089-2482]. Therefore, a further heat treatment at 550°C for 6 h was performed,

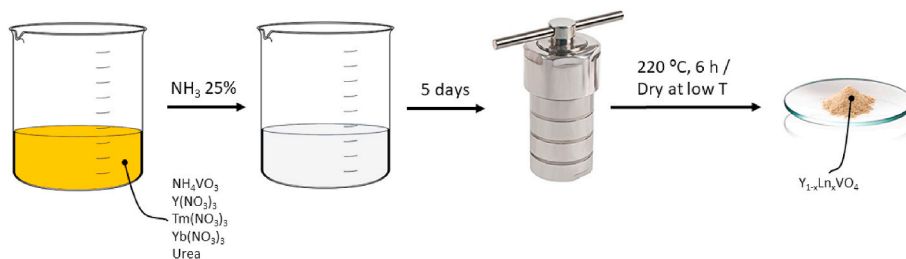


Fig. 1. Scheme reaction of the hydrothermal synthesis process.

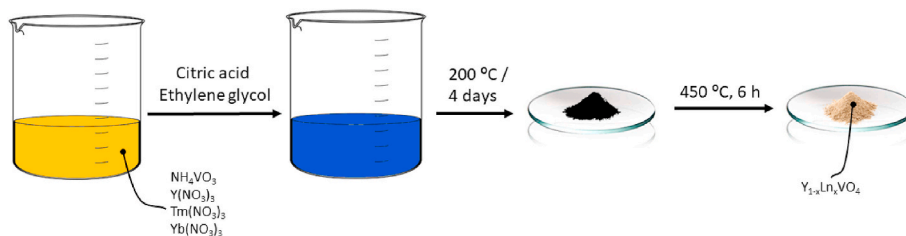
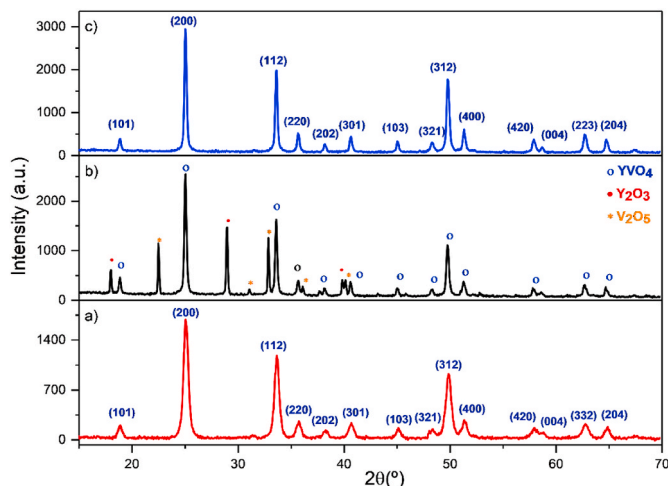


Fig. 2. Scheme reaction of the sol-gel process.

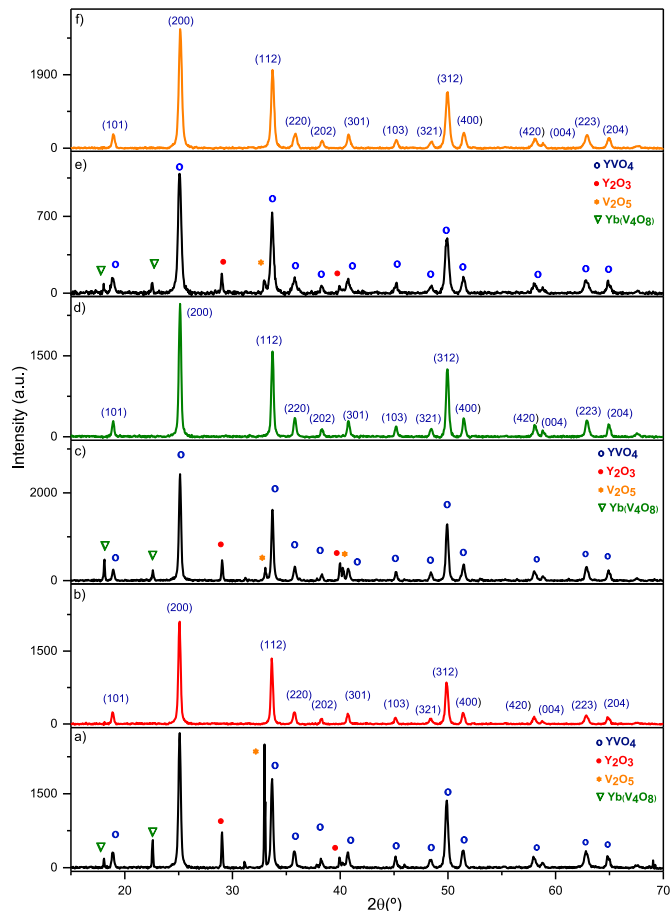
Fig. 3. XRD patterns of samples: (a) $Y_{0.9}Tm_{0.1}VO_4$ -SG at 450 °C, (b) $Y_{0.9}Tm_{0.1}VO_4$ -HT at 220 °C and (c) $Y_{0.9}Tm_{0.1}VO_4$ -HT at 550 °C.

and the diffraction profile shows a pure YVO_4 phase after this treatment. In the XRD profiles of $Y_{0.9}Tm_{0.1}VO_4$ -SG sample calcined at 450 °C and of $Y_{0.9}Tm_{0.1}VO_4$ -HT sample treated at 550 °C, the observed reflections can be indexed to a tetragonal symmetry of space group $I4_1/amd$ with $Z = 4$ [JCPDS file card n° 01-082-1968], compatible with the zircon-type structure of YVO_4 oxide. Thus, the purity of the obtained sample was confirmed.

Comparing the XRD patterns of the two pure samples, more intense reflections are found in the profile of $Y_{0.9}Tm_{0.1}VO_4$ -HT sample (Fig. 3c), indicating that this sample is more crystalline than the $Y_{0.9}Tm_{0.1}VO_4$ -SG sample (Fig. 3a), which was obtained by heating to lower temperature [12].

XRD patterns of $Y_{0.9}Tm_{0.1-x}Yb_xVO_4$ samples with $x = 0.01, 0.05, 0.09$ are shown in Fig. 4. Similarly, XRD profiles of samples prepared by hydrothermal synthesis at 220 °C reveal the presence of a mixture of phases. These phases are of the same oxides that have already been described in XRD profiles of Fig. 3. In the same way, all the diffraction maxima observed in the diffraction profiles of samples treated at 550 °C can be indexed to a tetragonal symmetry of $I4_1/amd$ space group of zircon structure of YVO_4 oxide, with $Z = 4$ [JCPDS file card n° 01-082-1968].

Lattice parameters and cell volume of all synthesized pure samples were calculated from XRD profiles of Figs. 3 and 4 using the Checkcell software [70,71]. As can be seen in Table 1, the determined parameters are slightly lower than the theoretical parameters of the YVO_4 oxide. This result can be explained considering the value of the Shannon ionic radii of the cations involved in the formula and located in an octa-coordinated environment of bisphenoids: Y^{3+} (1.019 Å), Tm^{3+} (0.994 Å) and Yb^{3+} (0.985 Å). Therefore, a smaller size of the thulium and ytterbium ions justifies a smaller value of cell parameters determined in the doped samples [72].

Fig. 4. XRD patterns of samples (a) $Y_{0.9}Tm_{0.09}Yb_{0.01}VO_4$ -HT at 220 °C; (b) $Y_{0.9}Tm_{0.09}Yb_{0.01}VO_4$ -HT at 550 °C; (c) $Y_{0.9}Tm_{0.05}Yb_{0.05}VO_4$ -HT at 220 °C; (d) $Y_{0.9}Tm_{0.05}Yb_{0.05}VO_4$ -HT at 550 °C; (e) $Y_{0.9}Tm_{0.01}Yb_{0.09}VO_4$ -HT at 220 °C and (f) $Y_{0.9}Tm_{0.01}Yb_{0.09}VO_4$ -HT at 550 °C.Table 1
Crystallographic parameters and average crystalline size of Tm^{3+} doped samples.

Sample	a = b (Å)	c (Å)	V (Å ³)	D (nm)
YVO_4 ^{aa}	7.1183	6.2893	318.7	—
$Y_{0.9}Tm_{0.1}VO_4$ -SG	7.096 (0)	6.250 (9)	314.8	20.2
$Y_{0.9}Tm_{0.1}VO_4$ -HT	7.098 (0)	6.277 (4)	316.3	34.3
$Y_{0.9}Tm_{0.09}Yb_{0.01}VO_4$ -HT	7.101 (5)	6.272 (9)	318.7	32.9
$Y_{0.9}Tm_{0.05}Yb_{0.05}VO_4$ -HT	7.092 (3)	6.266 (8)	314.8	34.3
$Y_{0.9}Tm_{0.01}Yb_{0.09}VO_4$ -HT	7.091 (7)	6.264 (1)	316.3	26.5

^a JCPDS file card n° 01-082-1968.

In addition, considering the most intense diffraction maxima corresponding to the (200), (112) and (312) planes and using the Scherrer equation (Eq. (1)) [69], an average crystalline size, D , was estimated for all synthesized samples (see Table 1). D values between 26.5 and 34.3 nm were determined for samples prepared by hydrothermal synthesis, while a slightly lower value of 20.2 nm was found for $Y_{0.9}Tm_{0.1}VO_4$ -SG sample. This result confirms the nanocrystalline character of the particles in these samples, in agreement with a higher intensity of the diffraction maxima observed in the XRD patterns of samples prepared by hydrothermal synthesis.

As previously stated, pure synthesized samples crystallize in a zircon-type structure (see Fig. 5) forming polyhedrals called 'bisdisphenoids'. In this structure, the lanthanide ions are randomly distributed being coordinated with eight oxygen atoms, while vanadium atoms are in tetrahedral positions. Thus, the structure can be described by means of zig-zag chains of bisdisphenoids linked by edges running along the a -axis. These chains are linked by VO_4^{3-} tetrahedra with which they share edges.

For comparative purposes, XRD patterns of some non-covered and silica-covered samples are shown in Fig. 6. A broad signal between $2\theta = 19$ – 24° is observed in XRD patterns of silica-covered samples, which confirms the presence of amorphous silica in these samples, in good agreement with previous reports by M. Rapp et al. [12].

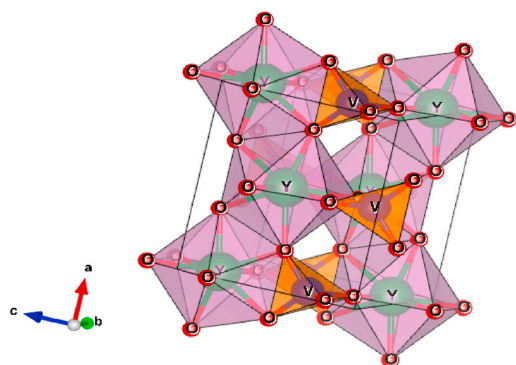


Fig. 5. Unit cell of the zircon-type structure of prepared samples which was generated with VESTA program [73]. Lanthanide ions are randomly distributed on the yttrium sites.

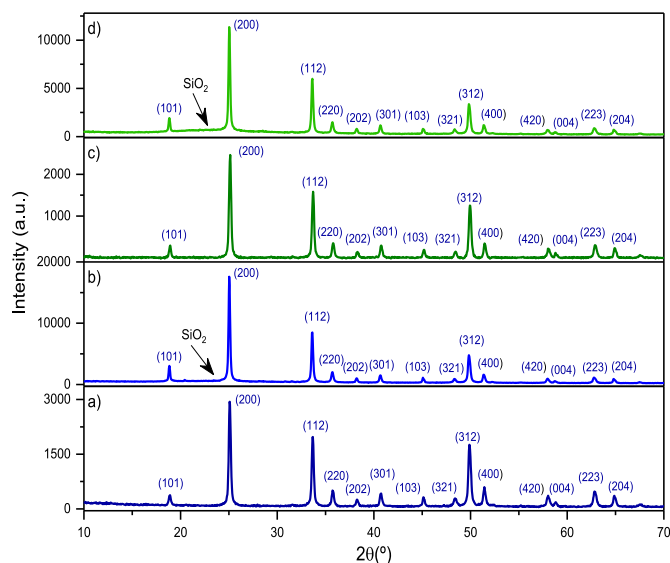


Fig. 6. XRD patterns of samples: (a) $Y_{0.9}Tm_{0.1}VO_4$ -HT, (b) $Y_{0.9}Tm_{0.1}VO_4$ -HT@ SiO_2 , (c) $Y_{0.9}Tm_{0.05}Yb_{0.05}VO_4$ -HT and (d) $Y_{0.9}Tm_{0.05}Yb_{0.05}VO_4$ -HT@ SiO_2 .

3.2. FTIR spectroscopy study

FTIR spectra of some uncoated and silica-coated samples are shown in Fig. 7.

Two main bands are observed in the FTIR spectra of non-covered samples. The first one appears at 450 cm^{-1} with weak-medium intensity, and it can be assigned to the antisymmetric stretching vibration of the $Y/Tm^{3+}/Yb^{3+}$ -O bonds [74,75], while the second one is a very strong and broad band around 780 cm^{-1} that can be assigned to the antisymmetric stretching vibrational mode of the V-O bonds in the VO_4^{3-} vanadate groups [45,76,77].

Compared to the FTIR spectra of uncoated samples, the spectra of coated samples show additional bands at $1072/1077\text{ cm}^{-1}$ with a shoulder at 1220 cm^{-1} assignable to the Si-O-Si and O-Si-O stretching vibrational modes, respectively [45,78]. It is noted that the absorption band at $450/452\text{ cm}^{-1}$ is remarkably more intense with the coating, due to the overlapping with the Si-O bending vibration that appears centered between 468 and 453 cm^{-1} [78,79].

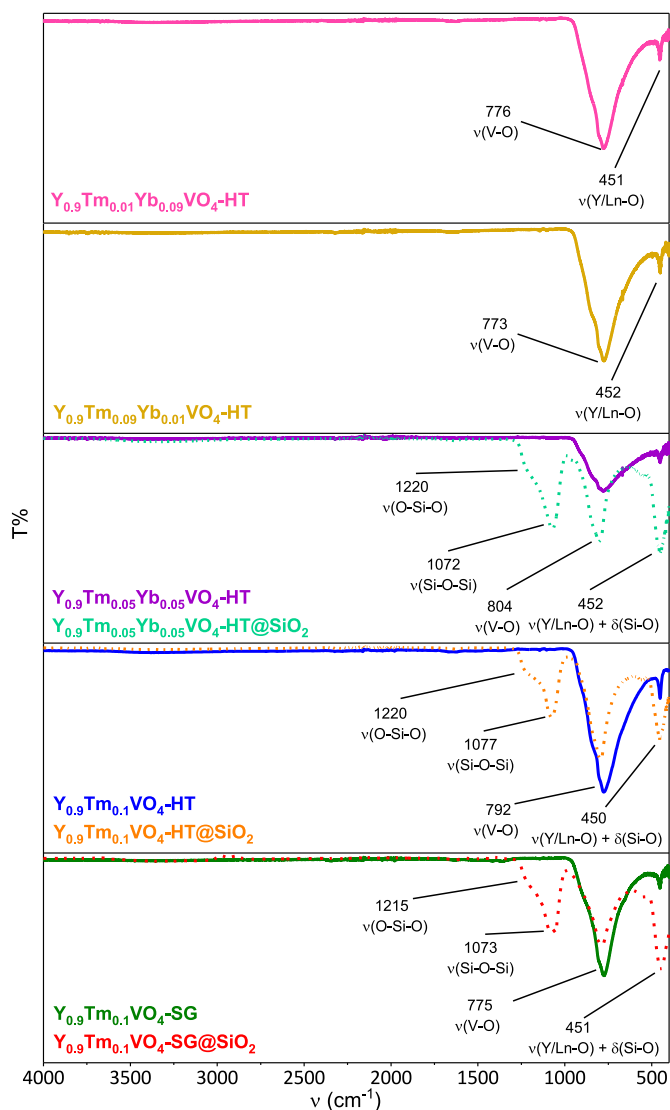


Fig. 7. FTIR spectra of the uncoated and silica-coated samples.

3.3. Transmission electron microscopy study

TEM images of the $Y_{0.9}Tm_{0.1}VO_4$ -SG, $Y_{0.9}Tm_{0.1}VO_4$ -HT and $Y_{0.9}Tm_{0.05}Yb_{0.05}VO_4$ -HT samples before and after reaction with TEOS are shown in Fig. 8. In the powder of $Y_{0.9}Tm_{0.1}VO_4$ -SG sample (Fig. 8e), irregular-rounded particles of smaller size and with dimensions between 11 and 20 nm can be observed, in good agreement with the average crystalline size calculated with Scherrer's equation (20 nm). By contrast, TEM images of $Y_{0.9}Tm_{0.1}VO_4$ -HT and $Y_{0.9}Tm_{0.05}Yb_{0.05}VO_4$ -HT samples (see Fig. 8a and c) shows particles of rounded and elongated morphologies with dimensions between 107×57 and 49×40 nm, and between 108×55 and 84×58 nm, respectively. These particle sizes differ from those calculated with the Scherrer equation (34.3 nm), which assumes that all particles are spherical [69], and as has been confirmed, this is not our case. From these results, it should be noted that the presence of urea in the reaction medium gives rise to powders of smaller particles, and this is justified by the large number of gases that are released during its synthesis [67]. The higher monodispersity of sizes in the sample prepared by the sol-gel method is attributed to the fact that, with this method, both size and morphology are better controlled than with the hydrothermal method. With the sol-gel method, an amorphous network is being formed during gel formation, which will subsequently drive the formation of the nanoparticles when the organic matter is calcined. On

the other hand, in the hydrothermal method there is a worse control of the morphology because the precursors simply react inside the autoclave. In addition, urea combustion accelerates the formation of nanoparticles and may affect the monodispersity due to the consequent higher reaction rate. This type of morphology has been published previously by our research group for similar orthovanadate samples prepared by this urea-assisted hydrothermal method [12].

After TEOS reaction, a silica shell of thickness between 18 and 22 nm is observed in TEM image of $Y_{0.9}Tm_{0.1}VO_4$ -SG@SiO₂ sample (Fig. 8f), while this thickness is somewhat lower, between 8 and 13 nm in TEM images of $Y_{0.9}Tm_{0.1}VO_4$ -HT@SiO₂ and $Y_{0.9}Tm_{0.05}Yb_{0.05}VO_4$ -HT@SiO₂ samples (see Fig. 8b and d). The increased thickness of silica shell around the smallest irregular rounded particles is remarkable. In all cases, these results confirm that the TEOS coating tests were successful, and that a thin silica shell was incorporated in the environment of individualized particles, in good agreement with previous investigations carried out in our research group [80].

The X-ray energy dispersive spectroscopy (XEDS) analyses (see Fig. 8 supp.) agree with the sample compositions and show a higher percentage of silica in the sample that is prepared by sol-gel (48.07 vs 72.06). This effect is also visualized in the thickness of the TEM images, see Fig. 8.

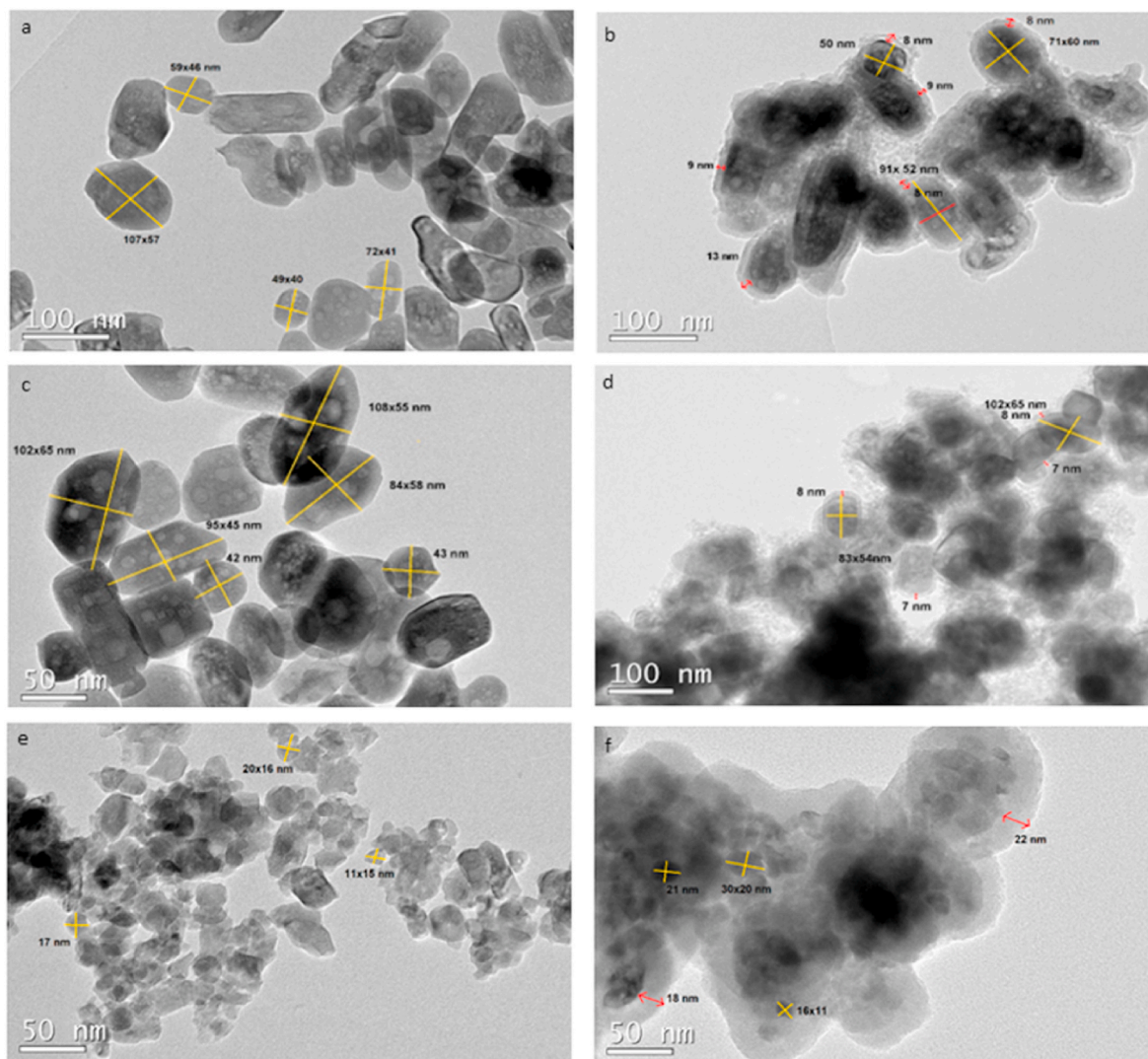


Fig. 8. TEM images of samples: (a) $Y_{0.9}Tm_{0.1}VO_4$ -HT, (b) $Y_{0.9}Tm_{0.1}VO_4$ -HT@SiO₂, (c) $Y_{0.9}Tm_{0.05}Yb_{0.05}VO_4$ -HT, (d) $Y_{0.9}Tm_{0.05}Yb_{0.05}VO_4$ -HT@SiO₂, (e) $Y_{0.9}Tm_{0.1}VO_4$ -SG and (f) $Y_{0.9}Tm_{0.1}VO_4$ -SG@SiO₂

3.4. Optical properties study

3.4.1. Absorption spectra

Prior to the fluorescence mechanisms study, an analysis of the absorption process is necessary to determine the optimal excitation wavelengths. For this reason, the absorption spectra of all samples were recorded within the biological windows spectral range (600–1700 nm) because a goal of the present study was to confirm their applicability in bioimaging. As an example, absorption spectra of $Y_{0.9}Tm_{0.1}VO_4$ -HT and $Y_{0.9}Tm_{0.05}Yb_{0.05}VO_4$ -HT samples are shown in Fig. 9.

A broad band around 1000 nm can be observed in the absorption spectra of $Y_{0.9}Tm_{0.1}VO_4$ -HT sample, which can be assigned to the $4f-4f$ electronic transitions of Tm^{3+} ions. By contrast, two bands around 800 and 1200 nm were observed in the absorption spectra of $Y_{0.9}Tm_{0.05}Yb_{0.05}VO_4$ -HT sample, which can be assigned to the $^3H_6-^3H_4$ and $^3H_6-^3H_5$ electronic transitions of Tm^{3+} ions, together with an absorption band at 980–1000 nm, assignable to the $^2F_{7/2} \rightarrow ^2F_{5/2}$ transition

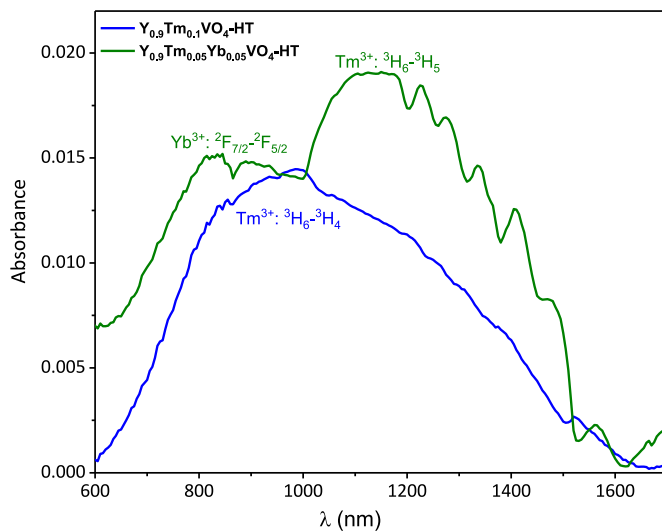


Fig. 9. Absorption spectra of $Y_{0.9}Tm_{0.1}VO_4$ -HT and $Y_{0.9}Tm_{0.05}Yb_{0.05}VO_4$ -HT samples measured in the NIR range.

of Yb^{3+} [37,81]. Lisiecki et al. [81] studied the absorption of Tm^{3+} in the YVO_4 host and they observed two bands around 800 and 1200 nm corresponding to the $^3H_6-^3H_4$ and $^3H_6-^3H_5$ electronic transitions of Tm^{3+} ions. The bands described by Lisiecki et al. were more clearly observed in the $Y_{0.9}Tm_{0.05}Yb_{0.05}VO_4$ -HT sample, while the absorption band of $Y_{0.9}Tm_{0.1}VO_4$ -HT sample seems to indicate that both bands have overlapped to give rise to a single observable band around 1000 nm.

3.4.2. Fluorescent emission study

The emission spectra of investigates samples were measured by excitation at 790 and 980 nm wavelengths available in the measurement devices. These wavelength values are suitable for excitation after studying the absorption process, see Fig. 9.

3.4.2.1. Influence of the synthesis method on the fluorescence emission intensity. Photoluminescence (PL) spectra of $Y_{0.9}Tm_{0.1}VO_4$ -SG and $Y_{0.9}Tm_{0.1}VO_4$ -HT samples recorded after excitation at 790 nm are shown in Fig. 10.

In the PL spectra of Fig. 10, an intense emission band centered around 1463 nm is observed together with two weak emission bands at 1049 nm and 1584 nm. These bands can be assigned to the $^3H_4 \rightarrow ^3F_4$, $^1G_4 \rightarrow ^3H_4$ and $^1G_4 \rightarrow ^3F_{2,3}$ electronic transitions, respectively, which occur between the levels of the Tm^{3+} ions [82]. The luminescent emission intensity of these bands clearly depends on both the preparation method and the synthesis conditions. $Y_{0.9}Tm_{0.1}VO_4$ -HT sample shows a higher emission intensity than that prepared by sol gel, $Y_{0.9}Tm_{0.1}VO_4$ -SG. This reduction in emission intensity can be explained considering a higher temperature (550 °C) used to obtain $Y_{0.9}Tm_{0.1}VO_4$ -HT sample than the 450 °C with which the $Y_{0.9}Tm_{0.1}VO_4$ -SG sample was obtained. These different thermal treatments led to small nanoparticles (11–20 nm) with higher specific surface-volume ratio in $Y_{0.9}Tm_{0.1}VO_4$ -SG sample and larger nanoparticles (107×57 and 49×40 nm) in the $Y_{0.9}Tm_{0.1}VO_4$ -HT sample, as observed in TEM images of Fig. 8. The treatment applied to obtain the $Y_{0.9}Tm_{0.1}VO_4$ -HT sample seems to eliminate the presence of surface defects with respect to the $Y_{0.9}Tm_{0.1}VO_4$ -SG sample. As is known, these defects increase the non-radiative decay, reducing the efficiency of the luminescent emission [45]. In this case, the reduction of surface defects in $Y_{0.9}Tm_{0.1}VO_4$ -HT sample leads to an increase in its fluorescence emission intensity.

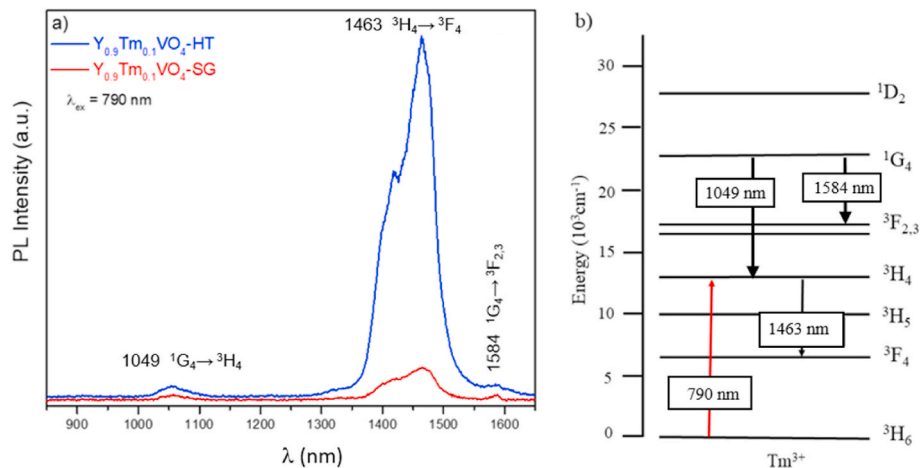


Fig. 10. (a) PL spectra of $Y_{0.9}Tm_{0.1}VO_4$ -HT and $Y_{0.9}Tm_{0.1}VO_4$ -SG samples. (b) Energy level diagram of Tm^{3+} ions.

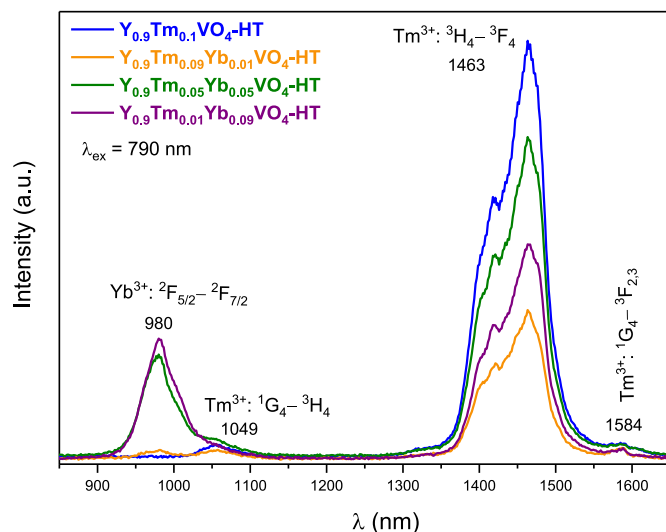


Fig. 11. PL spectra of $Y_{0.9}Tm_{0.1-x}Yb_xVO_4$ samples.

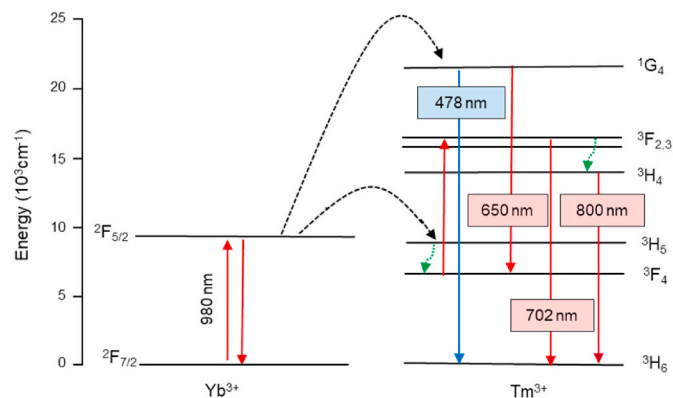


Fig. 12. Energy levels diagram of Yb^{3+}/Tm^{3+} and the UC process.

3.4.2.2. Influence of the substitution of thulium by ytterbium on the fluorescence emission intensity of $Y_{0.9}Tm_{0.1}Yb_xVO_4$ sample. PL spectra of $Y_{0.9}Tm_{0.1-x}Yb_xVO_4$ samples with $x = 0, 0.01, 0.05$ and 0.09 under excitation at 790 nm are shown in Fig. 11. Two emission bands can be clearly distinguished in these spectra. The strongest emission band around 1463 nm can be assigned to the $^3H_4 \rightarrow ^3F_4$ electronic transition of Tm^{3+} ions, while the emission band centered at 980 nm can be assigned to the $^2F_{5/2} \rightarrow ^2F_{7/2}$ electronic transition of Yb^{3+} ions [5,82,83]. In these spectra, two weak emission bands at 1049 nm and 1584 nm are also observed that can be assigned to the $^1G_4 \rightarrow ^3H_4$ and $^1G_4 \rightarrow ^3F_{2,3}$ electronic transitions of Tm^{3+} ions.

Analysis of the PL spectra in Fig. 11 reveals that the emission intensity of the band at 980 nm increases with ytterbium content. This feature is expected because this emission band is due to the electronic transition $^2F_{5/2} \rightarrow ^2F_{7/2}$ between the excited and ground levels of Yb^{3+} ions, see Fig. 12. By contrast, the emission intensity of the band at 1463 nm, assignable to the $^3H_4 \rightarrow ^3F_4$ electronic transition of Tm^{3+} ions, see Fig. 11, does not increase linearly with the ytterbium content, since it reaches a maximum of emission intensity for $Y_{0.9}Tm_{0.05}Yb_{0.05}VO_4$ sample. As can also be observed, higher ytterbium content quenches the fluorescence of Tm^{3+} ions, as reported elsewhere [84].

3.4.2.3. Influence of silica coating on the fluorescence emission intensity of $Y_{0.9}Tm_{0.1-x}Yb_xVO_4$ samples. Fig. 13 shows a comparison of the PL spectra

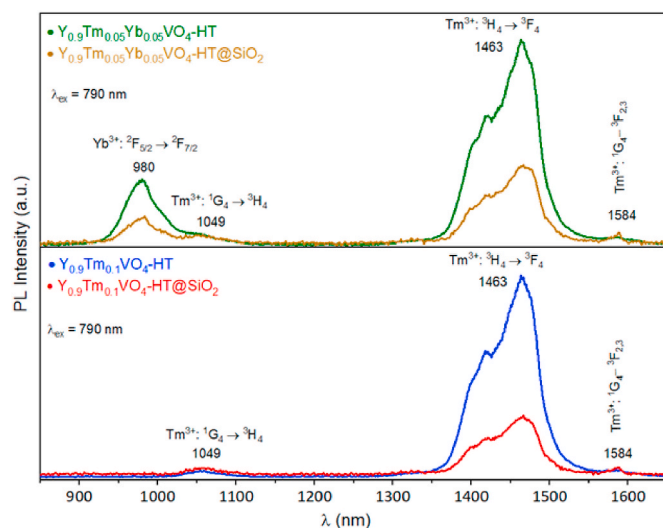


Fig. 13. PL spectra of non-covered and silica-coated $Y_{0.9}Tm_{0.1-x}Yb_xVO_4$ samples.

of some $Y_{0.9}Tm_{0.1-x}Yb_xVO_4$ samples under excitation at 790 nm. Again, the emission bands discussed above can be observed: a stronger emission band at 1463 nm together with two weaker emission bands at 1049 nm and 1584 nm in samples that do not contain ytterbium. In addition, an emission band centered at 980 nm in the $Y_{0.9}Tm_{0.05}Yb_{0.05}VO_4$ -HT sample (band assignment is included in the graph). In all cases, the emission intensity of the coated samples is reduced compared to the uncoated ones, although the emission intensity is still noticeable. This result can be justified considering the silica shell thickness surrounding the particles. As discussed above when comparing the emission intensity of $Y_{0.9}Tm_{0.1}VO_4$ -HT and $Y_{0.9}Tm_{0.1}VO_4$ -SG samples, the surface defects were significantly reduced in the sample obtained by hydrothermal synthesis. However, now the silica coating on the particles surface incorporates silanol groups that can act as a kind of quencher, causing a reduction of luminescent emission intensity [45–47], as can be seen in Fig. 13.

3.4.2.4. PL spectra analysis of Yb^{3+}/Tm^{3+} co-doped samples under excitation in the NIR region. PL spectra of Yb^{3+}/Tm^{3+} co-doped samples recorded under excitation at 980 nm and at $35^\circ C$ are shown in Fig. 14. The band at 800 nm assigned to the $^3H_4 \rightarrow ^3H_6$ electronic transition can be observed in the PL spectra of the three $Y_{0.9}Tm_{0.09}Yb_{0.01}VO_4$ -HT, $Y_{0.9}Tm_{0.05}Yb_{0.05}VO_4$ -HT and $Y_{0.9}Tm_{0.01}Yb_{0.09}VO_4$ -HT samples. In addition, typical blue and red emissions assignable to $^1G_4 \rightarrow ^3H_6$, $^1G_4 \rightarrow ^3F_4$ and $^3F_{2,3} \rightarrow ^3H_6$ electronic transitions of Tm^{3+} ions [41,82,84] are also observed, but only in the PL spectra of $Y_{0.9}Tm_{0.05}Yb_{0.05}VO_4$ -HT and $Y_{0.9}Tm_{0.01}Yb_{0.09}VO_4$ -HT samples. It is an expected result if the low content of ytterbium in the sample is considered, which does not favor the UC process. Comparatively, a higher ytterbium content, a higher emission intensity is observed in these samples, in good agreement with the UC process taking place after excitation.

The study of the fluorescence emission intensity in the NIR region is of great interest in the bioimaging field because the detection sensitivity of damaged cells increases in this range. In addition, the suppression of photon scattering and autofluorescence in the NIR-II transparency window (1000 – 1700 nm) give rises to a better image contrast and higher spatial resolution [12].

The study of UC processes in Yb^{3+}/Tm^{3+} co-doped samples involves ET from sensitizing Yb^{3+} ions to Tm^{3+} ions (see Fig. 12) [41,84,85]. In this process, the Yb^{3+} ions absorb the 980 nm radiation photons to

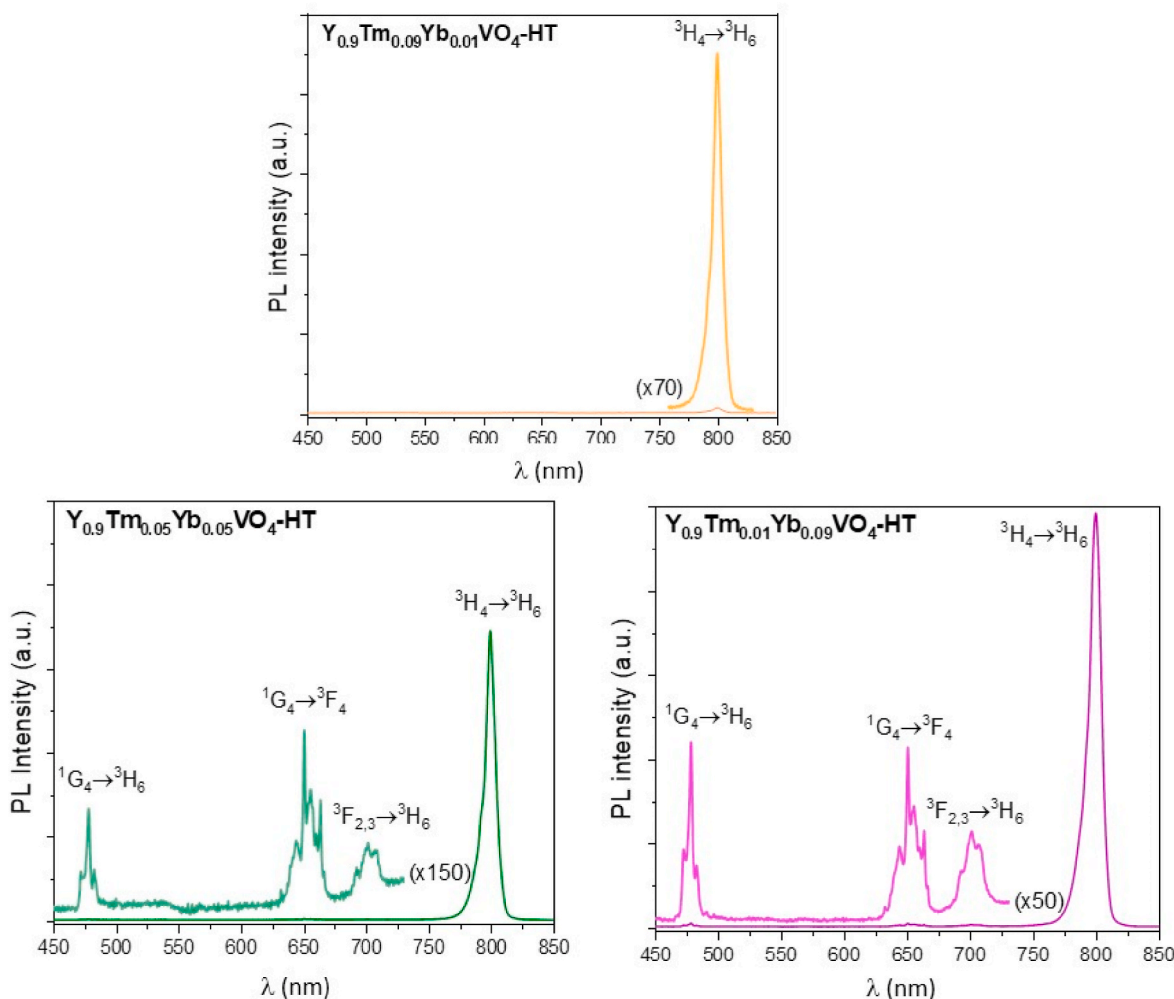


Fig. 14. PL spectra under excitation at 980 nm and at 35 °C of Yb³⁺/Tm³⁺ co-doped samples.

populate the $^2F_{5/2}$ excitation level. Then, with the help of more photons absorbed by these Tm³⁺ ions, the ET process takes place to populate the 3H_5 and 1G_4 excited states of Tm³⁺ ions [41,85]. From this 3H_5 level, a non-radiative relaxation occurs to 3F_4 level due to its short lifetime, and a subsequent rise to the excited $^3F_{2,3}$ level. The 3H_4 level is populated due to the non-radiative relaxation from $^3F_{2,3}$ level. Once the 1G_4 and $^3F_{2,3}$ levels are populated, typical blue ($^1G_4 \rightarrow ^3H_6$) and red ($^1G_4 \rightarrow ^3F_4$, $^3F_{2,3} \rightarrow ^3H_6$) electronic transitions of Tm³⁺ ions are observed at 478, 650 and 702 nm, respectively [41,82,84]. Additionally, the most intense band centered at 800 nm can be assigned to the $^3H_4 \rightarrow ^3H_6$ transition [40, 84].

3.4.2.5. Assessment of Yb³⁺/Tm³⁺ silica coated samples as fluorescent nanothermometers. Considering the greater biocompatibility of the silica coated samples related to the uncoated ones and that they also present a still noticeable fluorescent emission intensity, a study was carried out to evaluate their use as fluorescent thermometers.

PL spectra of Yb³⁺/Tm³⁺ silica coated samples registered under 980 nm excitation at five different temperatures (35, 38, 41, 44 and 47 °C) are shown in Fig. 15. In all cases, the same emission bands described above are observed.

A decrease in emission intensity can be observed as temperature increases in all PL spectra of Fig. 15. This result can be explained based on thermal extinction phenomenon that occurs with increasing temperature, since the atoms vibrate more in their lattice positions, and this hinders the ET from the sensitizing ion to the activator [40]. In addition, it can be explained by a higher energy absorption of the phonons at

higher temperature [41]. Comparatively, it is also observed that a higher UC emission intensity is reached by increasing the sensitizer ion content, as shown in Fig. 15 [84,85]. In Fig. 16 it can be seen clearly what has been discussed above: UC emission intensity decreases in all bands with increasing temperature. Additionally, from this representation it can be seen that the decrease in intensity as a function of temperature follows a different pattern depending on the sample, i.e., on the concentration of Tm³⁺ and Yb³⁺ ions. While in the Y_{0.9}Tm_{0.01}Yb_{0.09}VO₄-HT@SiO₂ sample the band emission decreases in a more linear way (or stepwise in the case of the 800 nm band), in Y_{0.9}Tm_{0.05}Yb_{0.05}VO₄-HT@SiO₂ sample the band emission seems to decrease exponentially.

The evaluation of these samples as fluorescent thermometers was carried out considering the PL spectra of Y_{0.9}Tm_{0.05}Yb_{0.05}VO₄-HT@SiO₂ and Y_{0.9}Tm_{0.01}Yb_{0.09}VO₄-HT@SiO₂ samples recorded between 35 and 47 °C. Sample Y_{0.9}Tm_{0.09}Yb_{0.01}VO₄-HT@SiO₂ sample was only measured at three representative temperatures, since it offers the worst response to the UC process and would not be the most suitable for use as a fluorescent thermometer. The temperature range was chosen to select the most suitable sample for *in vivo* assays, because these are the temperatures reached by healthy and diseased cells.

The fluorescence intensity ratio (FIR) is usually based on thermal coupling levels using the 3H_4 and $^3F_{2,3}$ excited levels. However, at temperatures close to room temperature and below 400 K, the emission at 702 nm ($^3F_{2,3} \rightarrow ^3H_6$) shows low intensity (see Fig. 12). This feature is because the thermal energy between these levels is too small to allow electrons to move easily in the narrow temperature range in which UC measurements were made. However, the non-thermal coupling energy

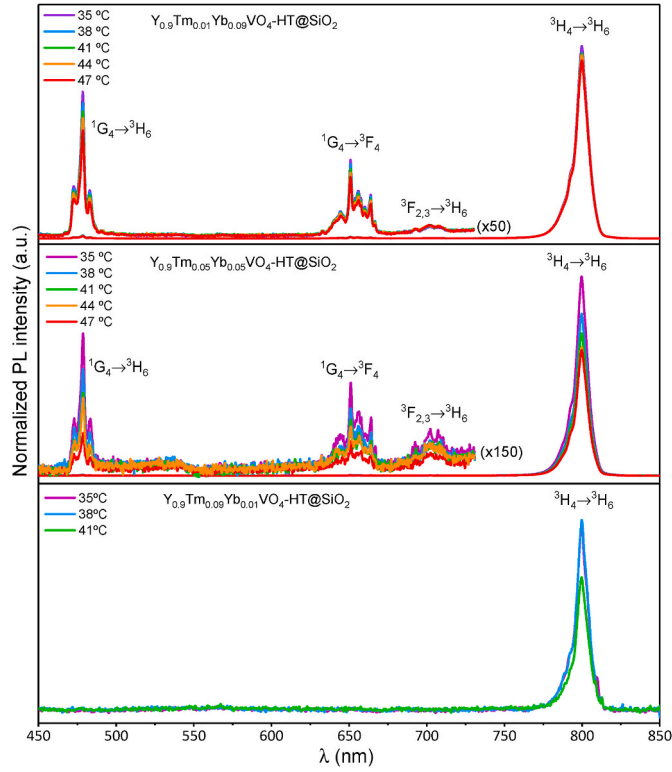


Fig. 15. PL spectra of $\text{Yb}^{3+}/\text{Tm}^{3+}$ silica coated samples. The second and third spectra have been normalized to the 650 nm peak.

levels (NTCL) also show temperature-dependent characteristics and are predominant in Ln^{3+} ions, so they can be used as thermal sensors [41]. The $^1\text{G}_4$ and $^3\text{F}_{2,3}$ levels are an example of NTCLs of Tm^{3+} ions. Both energy levels are separated by more than 2000 cm^{-1} ($\sim 6000 \text{ cm}^{-1}$), thus they do not have a temperature dependence following Boltzmann's law as reported with the $^3\text{H}_4$ and $^3\text{F}_{2,3}$ levels [85]. Taking the above into account, it can be observed (Fig. 15b and c) that the bands at 650 and 800 nm decrease in intensity with increasing temperature, this reduction being more pronounced in the band at 650 nm. This happens because the NTCLs between $^1\text{G}_4$ and $^3\text{H}_4$ are difficult to populate by thermal

excitation due to the large energy difference between them. Therefore, the temperature dependent FIR of these excited levels can be fitted by a polynomial function [41,85]:

$$\text{FIR} = \frac{I_{800}}{I_{650}} = A + BT + CT^2 + DT^3 \quad (6)$$

where I_{800} and I_{650} are the emission intensities of the 800 and 650 nm bands, respectively, and A, B, C and D are constants.

The experimental FIR (I_{800}/I_{650}) of the $\text{Y}_{0.9}\text{Tm}_{0.05}\text{Yb}_{0.05}\text{VO}_4\text{-HT@SiO}_2$ and $\text{Y}_{0.9}\text{Tm}_{0.01}\text{Yb}_{0.09}\text{VO}_4\text{-HT@SiO}_2$ samples was fitted by Eq. (6), as shown in Fig. 17. The equations that define a good fit were the following, respectively:

$$\text{FIR} = -(1.83 \pm 0.03) \cdot 10^6 + (1.76 \pm 0.03) \cdot 10^4 \cdot T - (56.6 \pm 0.9) \cdot T^2 + (6.06 \pm 0.09) \cdot 10^{-2} \cdot T^3$$

$$\text{FIR} = (6 \pm 2) \cdot 10^5 - (5 \pm 2) \cdot 10^3 \cdot T + (17 \pm 7) \cdot T^2 - (1.8 \pm 0.7) \cdot 10^{-2} \cdot T^3$$

As the thermal sensitivity (S) measures the temperature variation of the FIR, this can be expressed as shown in Eq. (7) [41,85].

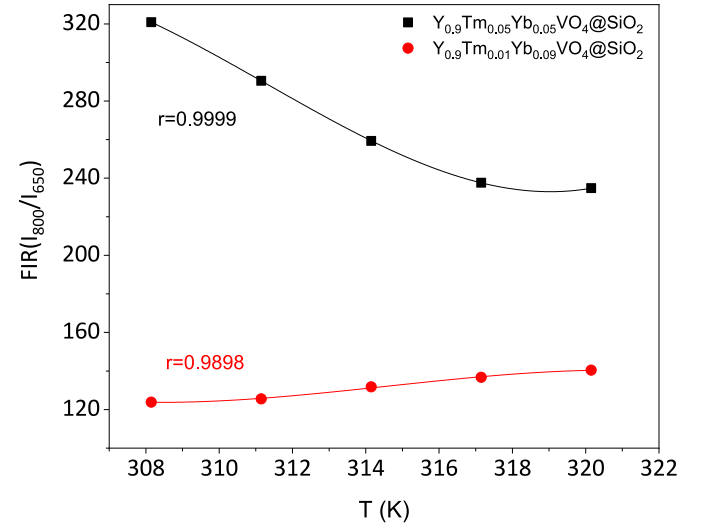


Fig. 17. FIR vs. temperature for silica coated $\text{Yb}^{3+}/\text{Tm}^{3+}$ co-doped samples.

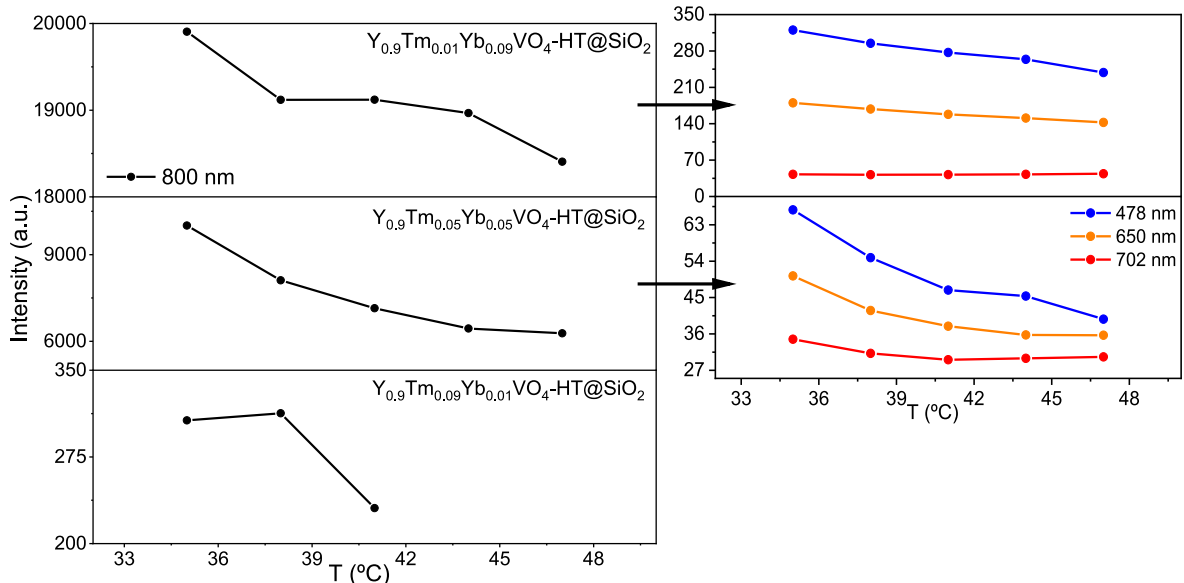


Fig. 16. Variation of the intensity with the temperature of all emission bands of the different silica coated samples.

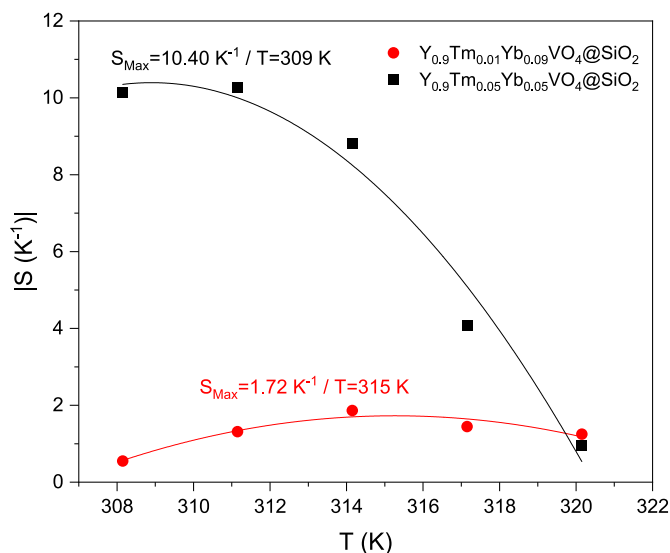


Fig. 18. Thermal sensitivity vs. temperature of silica coated $\text{Yb}^{3+}/\text{Tm}^{3+}$ co-doped samples.

$$|S(\text{K}^{-1})| = \left| \frac{d(\text{FIR})}{dT} \right| = B + 2CT + 3DT^2 \quad (7)$$

The maximum thermal sensitivity for both samples can be calculated from data of Fig. 18, obtaining values of 10.40 and 1.72 K^{-1} for the $\text{Y}_{0.9}\text{Tm}_{0.01}\text{Yb}_{0.09}\text{VO}_4\text{-HT@SiO}_2$ at 309 K and $\text{Y}_{0.9}\text{Tm}_{0.05}\text{Yb}_{0.05}\text{VO}_4\text{-HT@SiO}_2$ at 315 K samples, respectively.

These thermal sensitivity values are significantly higher than those reported in the literature for other thulium and ytterbium doped materials [40,85]. Note that the reported values refer to inorganic hosts other than YVO_4 . In the case of the samples investigated in this work, it can be observed that the thermal sensitivity increases with the ytterbium content. Therefore, these results show that the investigated samples are suitable as fluorescent thermometers within the physiological temperature range.

4. Conclusions

In the search for new materials of high quantum efficiency and of interest in the bioimaging field, $\text{Y}_{0.9}\text{Tm}_{0.1-x}\text{Yb}_x\text{VO}_4$ samples with $x = 0, 0.01, 0.05$ and 0.09 were successfully obtained as pure phases using hydrothermal synthesis with urea addition. For comparative purposes, a $\text{Y}_{0.9}\text{Tm}_{0.1-x}\text{Yb}_x\text{VO}_4$ sample was also prepared by sol-gel method. X-ray diffraction patterns confirm the zircon-type structure of the synthesized samples, in good agreement with FTIR spectra. Particles of spherical and elongated morphologies with dimensions between 107×57 and 49×40 nm, or 108×55 and 84×58 nm, were found in the TEM images of uncoated samples, while irregular-rounded particles of smaller size between 11 and 20 nm are found in the sample synthesized by the sol-gel method. A shell of 8–13 nm thickness was found in silica-coated samples. This shell is somewhat thicker in $\text{Y}_{0.9}\text{Tm}_{0.1}\text{VO}_4\text{-SG}$ sample. Characteristic bands of the Tm^{3+} and Yb^{3+} ions are found in the absorption and emission spectra of all synthesized samples with emission in the NIR and visible ranges. Substitution of Tm^{3+} by Yb^{3+} ions leads to higher UC emission under stimulation at 980 nm due to the increase population of the excited $^2\text{F}_{5/2}$ level, and a decrease in the $^3\text{H}_4$ level of Tm^{3+} ions. Based on the greater biocompatibility of silica coated $\text{Yb}^{3+}/\text{Tm}^{3+}$ co-doped samples, the study found higher thermal sensitivity values than those of other thulium and ytterbium doped materials described in the literature. The results obtained indicate that these samples are suitable for use as fluorescent thermometers within the temperature range of biological tissues.

Author statement

Y. Lozano: Investigation. J. Isasi: Investigation, Supervision, Draft preparation and revision. M. Fernández-Ramos: Investigation, Draft preparation and revision, sending paper. M. Rapp: Investigation, Draft preparation and revision. M. Alcolea Palafox: Manuscript revision. E. Ortiz-Rivero: Manuscript revision, software images. T. Muñoz-Ortiz: Manuscript revision, software images.

Declaration of competing interest

The authors declare that they have no known competing financial interests or personal relationships that could have appeared to influence the work reported in this paper.

Data availability

The authors do not have permission to share data.

Acknowledgements

This work was financially supported by the Spanish Ministry of Science and Innovation, through projects PID2019-106211RB-I00 and PID2019-105195RA-I00, the Instituto de Salud Carlos III (PI19/00565), by the Comunidad Autónoma de Madrid (S2017/BMD-3867RENIMCM) co-financed by the European structural and investment fund, and by Universidad Autónoma de Madrid and Comunidad Autónoma de Madrid (SI1/PJI/2019-00052). E.O.R gratefully acknowledges the financial support provided by the Spanish Ministerio de Universidades, through the FPU program (FPU19/04803).

Appendix A. Supplementary data

Supplementary data to this article can be found online at <https://doi.org/10.1016/j.jlumin.2023.119708>.

References

- [1] D. Kim, Recent developments in lanthanide-doped alkaline earth aluminate phosphors with enhanced and long-persistent luminescence nanomaterials, *Nanomaterials* 11 (2021) 723–750, <https://doi.org/10.3390/nano11030723>.
- [2] U.A. Bawane, A.R. Kadam, A. Nande, S.J. Dhoble, Critical review on lanthanide activated LED phosphors, *J. Phys.: Conf. Ser.* 1913 (2021), 012030, <https://doi.org/10.1088/1742-6596/1913/1/012030>.
- [3] R.M. Almeida, N. Sousa, R.E. Rojas-Hernández, L.F. Santos, Frequency conversion in lanthanide-doped sol-gel derived materials for energy applications, *J. Sol. Gel Sci. Technol.* 95 (2020) 520–529, <https://doi.org/10.1007/s10971-020-05289-w>.
- [4] A. Tiwari, S.J. Dhoble, Tunable lanthanide/transition metal ion-doped novel phosphors for possible application in w-LEDs: a review, *J. Biol. Chem. Lumin.* 35 (2019) 4–33, <https://doi.org/10.1002/bio.3712>.
- [5] G.Q. Wang, B.W. Liu, Y.P. Lin, Y. Shi, R. Ye, L.Y. Li, Color-tunable upconversion luminescence in novel lanthanum borogermanates for optical thermometry application, *J. Alloys Compd.* 826 (2020), 153274, <https://doi.org/10.1016/j.jallcom.2019.153274>.
- [6] S. Khan, Y.R. Parauha, D.K. Halwar, S.J. Dhoble, Rare earth (RE) doped color tunable phosphors for white light emitting diodes, *J. Phys.: Conf. Ser.* 1913 (2021), 012017, <https://doi.org/10.1088/1742-6596/1913/1/012017>.
- [7] T.S. Sreena, P. Prabhakar Rao, T.R. Aju Thara, A.K.V. Raj, New lanthanide-free self-activated full-color emission phosphor in Y^{3+} doped $\text{Sr}_3\text{Bi}(\text{VO}_4)_3$ system for white light emitting diode applications, *Luminescence* 36 (2021) 819–825, <https://doi.org/10.1002/bio.4007>.
- [8] M.K. Mahata, R. De, K.T. Lee, Near-infrared-triggered upconverting nanoparticles for biomedicine applications, *Biomedicines* 9 (2021) 756–782, <https://doi.org/10.3390/biomedicines9070756>.
- [9] Y. Chen, J. Qiu, Z. Chen, Y. Zhao, B. Li, C. Zeng, New luminescent lanthanide complexes and Tb, Eu co-doped complex as a wide temperature self-calibrating thermometer, *Dyes Pigments* 194 (2021), 109671, <https://doi.org/10.1016/j.dyepig.2021.109671>.
- [10] K. Elzbiaciak-Piecka, M. Suta, L. Marciniak, Structurally induced tuning of the relative sensitivity of $\text{LaScO}_3:\text{Cr}^{3+}$ luminescent thermometers by co-doping lanthanide ions, *Chem. Eng. J.* 421 (2021), 129757, <https://doi.org/10.1016/j.cej.2021.129757>.
- [11] A.K. Maini, *Lasers and Optoelectronics: Fundamentals, Devices and Applications*, John Wiley & Sons, United Kingdom, 2013.

- [12] M. Rapp, J. Isasi, M. Alcolea, T. Muñoz, E. Ortiz-Rivero, Synthesis, structural and morphological characterization and photoluminescence study of $\text{Y}_{0.9}\text{Er}_{0.1-x}\text{Yb}_x\text{VO}_4$ materials, *J. Alloys Compd.* 903 (2022), 163930, <https://doi.org/10.1016/j.jallcom.2022.163930>.
- [13] D.K. Zharkov, A.G. Shmelev, A.V. Leontyev, V.G. Nikiforov, V.S. Lobkov, M. H. Alkahtani, P.R. Hemmer, V. V. Samartsev Light converting $\text{Yb}^{3+}/\text{Er}^{3+}$ doped YVO_4 nanoparticles for biological applications, *Laser Phys. Lett.* 17 (2020), 075901, <https://doi.org/10.1088/1612-202X/ab9115>.
- [14] I. Gupta, S. Singh, S. Bhagwan, D. Singh, Rare earth (RE) doped phosphors and their emerging applications: a review, *Ceram. Int.* 47 (2021) 19282–19303, <https://doi.org/10.1016/j.ceramint.2021.03.308>.
- [15] A. Dwivedi, D. Kumar, S.B. Rai, A.K. Rai, Effect of host on the radiative (upconversion emission) as well as non-radiative relaxation (laser induced optical heating) in $\text{Tm}^{3+}/\text{Yb}^{3+}$ co-doped phosphors, *J. Lumin.* 226 (2020), 117421, <https://doi.org/10.1016/j.jlumin.2020.117421>.
- [16] E. Kolobkova, A. Grabtchikov, I. Khodasevich, Upconversion luminescence and energy transfer in the fluorophosphate glasses with low phosphate content doped with Tm^{3+} and Yb^{3+} ions, *J. Non-Cryst. Solids X* 11 (2021), 100065, <https://doi.org/10.1016/j.nocx.2021.100065>.
- [17] B.R. Judd, Optical absorption intensities of rare-earth ions, *Phys. Rev.* 127 (1962) 750–761, <https://doi.org/10.1103/PhysRev.127.750>.
- [18] G.S. Ofelt, Intensities of crystal spectra of rare-earth ions, *J. Chem. Phys.* 37 (1962) 511–520, <https://doi.org/10.1063/1.1701366>.
- [19] L. Smentek, Judd–Ofelt theory: past, present and future, *Mol. Phys.* 101 (2003) 893–897, <https://doi.org/10.1080/0026897021000046717>.
- [20] J.G. Bünzli, C. Piguet, Taking advantage of luminescent lanthanide ions, *Chem. Soc. Rev.* 34 (2005) 1048–1077, <https://doi.org/10.1039/B406082M>.
- [21] L. Smentek, Theoretical description of the spectroscopic properties of rare earth ions in crystals, *Phys. Rep.* 297 (1998) 155–237, [https://doi.org/10.1016/S0370-1573\(97\)00077-X](https://doi.org/10.1016/S0370-1573(97)00077-X).
- [22] A. Ćirić, S. Stojadinović, M.D. Dramićanin, An extension of the Judd–Ofelt theory to the field of lanthanide thermometry, *J. Lumin.* 216 (2019), 116749, <https://doi.org/10.1016/j.jlumin.2019.116749>.
- [23] M. Ferhi, C. Bouzidi, K. Horchani-Naifer, H. Elhouichet, M. Ferid, Judd–Ofelt analysis of spectroscopic properties of Eu^{3+} doped $\text{KLa}(\text{PO}_3)_4$, *J. Lumin.* 157 (2015) 21–27, <https://doi.org/10.1016/j.jlumin.2014.08.017>.
- [24] Z. Guo, Z. Zhu, X. Zhang, L. Zhou, Photoluminescent properties and Judd–Ofelt analysis of Eu^{3+} -doped $\text{NaMg}(\text{PO}_3)_2$ red phosphor, *J. Lumin.* 202 (2018) 484–488, <https://doi.org/10.1016/j.jlumin.2018.06.020>.
- [25] S. Pei, X. Ge, L. Sun, Metal ions doping for boosting luminescence of lanthanide-doped nanocrystals, *Nanocrystals*. *Front. Chem.* 8 (2020), 610481, <https://doi.org/10.3389/fchem.2020.610481>.
- [26] C. Coteau, Spontaneous parametric down-conversion, *Contemp. Phys.* 59 (2018) 291–304, <https://doi.org/10.1080/00107514.2018.1488463>.
- [27] M.B. De la Mora, O. Amelines-Sarria, B.M. Monroy, C.D. Hernández-Pérez, J. E. Lugo, Materials for downconversion in solar cells: perspectives and challenges, *Sol. Energy Mater. Sol. Cells* 165 (2017) 59–71, <https://doi.org/10.1016/j.solmat.2017.02.016>.
- [28] W. Yang, X. Li, D. Chi, H. Zhang, X. Liu, Lanthanide-doped upconversion materials: emerging applications for photovoltaics and photocatalysis, *J. Nanotech.* 25 (2014), 482001, <https://doi.org/10.1088/0957-4484/25/48/482001>.
- [29] T. Sun, F. Ai, G. Zhu, F. Wang, Recent progress of upconversion nanostructured materials: from optical tuning to biomedical applications, *Chem. Asian J.* 13 (2018) 373–385, <https://doi.org/10.1002/asia.201701660>.
- [30] Q. Zou, P. Huang, W. Zheng, W. You, R. Li, D. Tu, J. Xu, X. Chen, Cooperative and non-cooperative sensitization upconversion in lanthanide-doped LiYbF_4 nanoparticles, *Nanoscale* 9 (2017) 6521–6528, <https://doi.org/10.1039/C7NR02124K>.
- [31] M. Haase, H. Schäfer, Upconverting nanoparticles, *Angew. Chem., Int. Ed. Engl.* 50 (2011) 5808–5829, <https://doi.org/10.1002/anie.201005159>.
- [32] S. Ye, G. Chen, W. Shao, J. Qu, P.N. Prasad, Tuning upconversion through a sensitizer/activator-isolated NaYF_4 core/shell structure, *Nanoscale* 7 (2015) 3976–3984, <https://doi.org/10.1039/C4NR07678H>.
- [33] A. Kar, S. Kundu, A. Patra, Lanthanide-doped nanocrystals: strategies for improving the efficiency of upconversion emission and their physical understanding, *ChemPhysChem* 16 (2015) 505–521, <https://doi.org/10.1002/cphc.201402668>.
- [34] D. Kang, E. Jeon, S. Kim, J. Lee, Lanthanide-doped upconversion nanomaterials: recent advantages and applications, *BioChip. J.* 14 (2020) 124–135, <https://doi.org/10.1007/s13206-020-4111-9>.
- [35] S. Wilhelm, Perspectives for upconverting nanoparticles, *ACS Nano* 11 (2017) 10644–10653, <https://doi.org/10.1021/acsnano.7b07120>.
- [36] Y. Zhong, Z. Ma, S. Zhu, J. Yue, M. Zhang, A.L. Antaris, H. Dai, Boosting the down-shifting luminescence of rare-earth nanocrystals for biological imaging beyond 1500 nm, *Nat. Commun.* 8 (2017) 1–7, <https://doi.org/10.1038/s41467-017-00917-6>.
- [37] K. Teshima, S. Lee, N. Shikine, T. Wakabayashi, K. Yubuta, T. Shishido, S. Oishi, S. Flux growth of highly crystalline NaYF_4 : Ln (Ln = Yb, Er, Tm) crystals with upconversion fluorescence, *J. Crystal Grow. & Des.* 11 (2011) 995–999, <https://doi.org/10.1021/cg100932k>.
- [38] L. Alcaraz, J. Isasi, Synthesis and study of $\text{Y}_{0.9}\text{Ln}_{0.1}\text{VO}_4$ nanophosphors and $\text{Y}_{0.9}\text{Ln}_{0.1}\text{VO}_4/\text{SiO}_2$ luminescent nanocomposites with Ln = Eu, Dy, Er, *Ceram. Int.* 43 (2017) 5311–5318, <https://doi.org/10.1016/j.ceramint.2017.01.069>.
- [39] B. Del Rosal, D. Jaque, Upconversion nanoparticles for *in vivo* applications: limitations and future perspectives, *Methods Appl. Fluoresc.* 7 (2019), 022001, <https://doi.org/10.1088/2050-6120/ab029f>.
- [40] M. Jia, Z. Sun, H. Xu, X. Jin, Z. Lv, T. Sheng, J.Z. Fu, An ultrasensitive luminescent nanothermometer in the first biological window based on phonon-assisted thermal enhancing and thermal quenching, *Mater. Chem. C* 8 (2020) 15603–15608, <https://doi.org/10.1039/D0TC04082G>.
- [41] X. Gao, W. Ge, J. Shi, X. Chen, Y. Li, A novel upconversion thermometers derived from non-thermal coupling levels of $\text{CaZnO}:\text{Sm}^{2+}/\text{Yb}^{3+}$ phosphors, *J. Solid State Chem.* 297 (2021), 122063, <https://doi.org/10.1016/j.jssc.2021.122063>.
- [42] P. Granger, V.I. Parvulescu, W. Prellier, Perovskites and related mixed oxides, in: *From Solid-State Chem. To Soft Chem. Routes*, 2016, pp. 1–24, <https://doi.org/10.1002/9783527686605.ch01>.
- [43] D.J. Jovanović, Lanthanide doped orthovanadate phosphors: syntheses, structures, and photoluminescence properties, *Woodhead Publ. ser. electron. opt. mater.* (2020) 235–291, <https://doi.org/10.1016/B978-0-08-102935-0.00006-X>.
- [44] C.H. Yan, Z.G. Yan, Y.P. Du, J. Shen, C. Zhang, W. Feng, Controlled synthesis and properties of rare earth nanomaterials, in: *Handbook on the Phys. And Chem. of Rare Earths*, 2011, pp. 275–472, <https://doi.org/10.1016/B978-0-444-53590-0.00004-2>.
- [45] L. Alcaraz, J. Isasi, C. Díaz-Guerra, Influence of the synthesis conditions of $\text{Y}_{0.9}\text{Dy}_{0.1}\text{VO}_4$ and silica-coated $\text{Y}_{0.9}\text{Dy}_{0.1}\text{VO}_4$ nanophosphors on the powder morphology and luminescence emission intensity, *J. Nanoparticle Res.* 21 (2019) 1–13, <https://doi.org/10.1007/s11051-019-4514-5>.
- [46] L. Alcaraz, J. Isasi, C. Díaz-Guerra, Effects of preparation method and pH variation on the structural characteristics and luminescence properties of $\text{Y}_{0.1}\text{Er}_{0.1}\text{VO}_4$ and $\text{Y}_{0.9}\text{Er}_{0.1}\text{VO}_{0.9}\text{Cr}_{0.1}\text{O}_4$ nanopowders, *J. Lumin.* 165 (2015) 105–114, <https://doi.org/10.1016/j.jlumin.2015.04.038>.
- [47] L. Alcaraz, J. Isasi, C. Díaz-Guerra, Comparative study of $\text{Y}_{0.9}\text{Er}_{0.1}\text{V}_{1-x}\text{P}_x\text{O}_4$ nanophosphors with $x=0, 0.1, 0.5, 0.9$ and 1 prepared by sol-gel and hydrothermal processes, *J. Alloys Compd.* 687 (2016) 754–764, <https://doi.org/10.1016/j.jallcom.2016.06.169>.
- [48] C.E. Rivera-Enriquez, A.L. Fernández-Osorio, Synthesis of YVO_4 : Eu^{3+} nanophosphors by the chemical coprecipitation method at room temperature, *J. Lumin.* 236 (2021), 118110, <https://doi.org/10.1016/j.jlumin.2021.118110>.
- [49] L. Mentasti, N. Martínez, I.A. Zucchi, M. Santiago, G. Barreto, Development of a simple process to obtain luminescent YVO_4 : Eu^{3+} nanoparticles for Fiber Optic Dosimetry, *J. Alloys Compd.* 829 (2020), 154628, <https://doi.org/10.1016/j.jallcom.2020.154628>.
- [50] M.A. Neouze, A.P. Freitas, R.K. Ramamoorthy, R. Mohammadi, E. Larquet, S. Tusseau-Nenez, D. Carrière, T. Gacoin, Toward a chemical control of colloidal YVO_4 nanoparticles microstructure, *Langmuir* 36 (2020) 9124–9131, <https://doi.org/10.1021/acs.langmuir.0c01266>.
- [51] M.N. Luwang, R.S. Ningthoujam, S.K. Srivastava, R.K. Vatsa, Preparation of white light emitting YVO_4 : Ln^{3+} and silica-coated YVO_4 : Ln^{3+} ($\text{Ln}^{3+} = \text{Eu}^{3+}, \text{Dy}^{3+}, \text{Tm}^{3+}$) nanoparticles by CTAB/n-butanol/hexane/water microemulsion route: energy transfer and site symmetry studies, *J. Math. Chem.* 21 (2011) 5326, <https://doi.org/10.1039/C0JM03470C>.
- [52] J. Shao, J. Yan, X. Li, S. Li, T. Hu, Novel fluorescent label based on YVO_4 : $\text{Bi}^{3+}, \text{Eu}^{3+}$ for latent fingerprint detection, *Dyes Pigments* 160 (2019) 555–562, <https://doi.org/10.1016/j.dyepig.2018.08.033>.
- [53] A. Luo, D. Guoping, L. Hongmei, S. Wangzhou, Photoluminescence of europium-doped and europium/strontium-codoped sol-gel-prepared yttrium vanadate nanoparticles, *Mater. Sci. Semicond. Process.* 23 (2014) 20–26, <https://doi.org/10.1016/j.mssp.2014.02.016>.
- [54] M. Yoshimura, J. Livage, Soft processing for advanced inorganic material, *MRS Bull.* 25 (2000) 12–13, <https://doi.org/10.1557/mrs2000.174>.
- [55] M. Yoshimura, K. Byrappa, Hydrothermal processing of materials: past, present and future, *J. Math. Sci.* 43 (2008) 2085–2103, <https://doi.org/10.1007/s10853-007-1853-x>.
- [56] J. Isasi, P. Arévalo, E. Martín, F. Martín-Hernández, Preparation and study of silica and APTES-silica-modified NiFe_2O_4 nanocomposites for removal of Cu^{2+} and Zn^{2+} ions from aqueous solutions, *J. Sol. Gel Sci. Technol.* 91 (2019) 596–610, <https://doi.org/10.1007/s10971-019-05067-3>.
- [57] P. Arévalo-Cid, J. Isasi, F. Martín-Hernández, Comparative study of core-shell nanostructures based on amino-functionalized $\text{Fe}_3\text{O}_4/\text{SiO}_2$ and $\text{CoFe}_2\text{O}_4/\text{SiO}_2$ nanocomposites, *J. Alloys Compd.* 766 (2018) 609–618, <https://doi.org/10.1016/j.jallcom.2018.06.246>.
- [58] I. Gonzalo-Juan, B. Ferrari, M.T. Colomer, Influence of the urea content on the YSZ hydrothermal synthesis under dilute conditions and its role as dispersant agent in the post-reaction medium, *J. Eur. Ceram. Soc.* 29 (2009) 3185–3195, <https://doi.org/10.1016/j.jeurceramsoc.2009.04.041>.
- [59] W. Stöber, A. Fink, E. Bohn, Controlled growth of monodisperse silica spheres in the micron size range, *J. Colloid Interface Sci.* 26 (1968) 62–69, [https://doi.org/10.1016/0021-9797\(68\)90272-5](https://doi.org/10.1016/0021-9797(68)90272-5).
- [60] P. Scherrer, Bestimmung der Größe und der inneren Struktur von Kolloidteilchen mittels Röntgenstrahlen. Nachrichten von der Gesellschaft der Wissenschaften zu Göttingen, Math Klasse 2 (1918) 98–100. <http://eudml.org/doc/59018>.
- [61] O. Dlugosz, K. Szostak, A. Starón, J. Pulit-Prociak, M. Banach, Methods for reducing the toxicity of metal and metal oxide NPs as biomedicine, *Materials* 13 (2020) 279–298, <https://doi.org/10.3390/ma13020279>.
- [62] N. Sounderya, Y. Zhang, Use of core/shell structured nanoparticles for biomedical applications, *Recent Pat. Biomed. Eng.* 1 (2008) 34–42, <https://doi.org/10.2174/1874764710801010034>.
- [63] R. Jenjob, T. Phakkeeree, D. Crespy, Core-shell particles for drug-delivery, bioimaging, sensing, and tissue engineering, *Biomater. Sci.* 8 (2020) 2756–2770, <https://doi.org/10.1039/C9BM01872G>.

- [64] K. Chatterjee, S. Sarkar, R. Jagajjani, P. Santanu, Core/Shell nanoparticles in biomedical applications, *J. Advan. Colloid Interface Sci.* 209 (2014) 8–39, <https://doi.org/10.1016/j.cis.2013.12.008>.
- [65] R. Xie, Y. Li, Z. Zhou, X. Pang, C. Wu, P. Yin, H. Li, A near-infrared excitation/emission fluorescent probe for imaging of endogenous cysteine in living cells and zebrafish, *Anal. Bioanal. Chem.* 412 (2020) 5539–5550, <https://doi.org/10.1007/s00216-020-02812-4>.
- [66] M. Rapp, Y. Lozano, M. Fernandez, J. Isasi, M. Alcolea Palafox, Superparamagnetic and light-emitting bifunctional nanocomposites of iron oxide and erbium or thulium doped yttrium orthovanadate, *J. Alloys Compd.* 929 (2022), 167065, <https://doi.org/10.1016/j.jallcom.2022.167065>.
- [67] I. Gonzalo-Juan, B. Ferrari, M.T. Colomer, Influence of the urea content on the YSZ hydrothermal synthesis under dilute conditions and its role as dispersant agent in the post-reaction medium, *J. Eur. Ceram. Soc.* 29 (2009) 3185–3195, <https://doi.org/10.1016/j.jeurceramsoc.2009.04.041>.
- [68] W. Stöber, A. Fink, E. Bohn, Controlled growth of monodisperse silica spheres in the micron size range, *J. Colloid Interface Sci.* 26 (1968) 62–69, [https://doi.org/10.1016/0021-9797\(68\)90272-5](https://doi.org/10.1016/0021-9797(68)90272-5).
- [69] P. Scherrer, Bestimmung der Größe und der inneren Struktur von Kolloidteilchen mittels Röntgenstrahlen. Nachrichten von der Gesellschaft der Wissenschaften zu Göttingen, Math Klasse 2 (1918) 98–100. <http://eudml.org/doc/59018>.
- [70] J. Prado-Gonjal, M.E. Villafuerte-Castrejón, L. Fuentes, E. Morán, Microwave-hydrothermal synthesis of the multiferroic BiFeO₃, *Mater. Res. Bull.* 44 (2009) 1734–1737, <https://doi.org/10.1016/j.materresbull.2009.03.015>.
- [71] J. Laugier, B. Bochu, Checkcell—a Software Performing Automatic Cell/Space Group Determination, Collaborative Computational Project Number 14 (CCP14), Laboratoire des Matériaux et du Génie Physique de l'Ecole Supérieure de Physique de Grenoble (INPG), France. <http://chemb191.chem.ucl.ac.uk/tutorial/lmgp/achekcell.htm>, 2000.
- [72] R.D. Shannon, C.T. Prewitt, Revised values of effective ionic radii, *Acta Crystallogr.* 26 (1970) 1046–1048, <https://doi.org/10.1107/S0567740870003576>.
- [73] K. Momma, F. Izumi, VESTA: a three-dimensional visualization system for electronic and structural analysis, *J. Appl. Crystallogr.* 41 (2008) 653–658, <https://doi.org/10.1107/S0021889808012016>.
- [74] R.S. Ningthoujam, L.R. Singh, V. Sudarsan, S. Dorendrajit Singh, Energy transfer process and optimum emission studies in luminescence of core-shell nanoparticles: YVO₄:Eu-YVO₄ and surface state analysis, *J. Alloys Compd.* 484 (2009) 782–789, <https://doi.org/10.1016/j.jallcom.2009.05.044>.
- [75] B.K. Grandhe, V.R. Bandi, K. Jang, S. Ramaprabhu, H.S. Lee, D.S. Shin, S.S. Yi, J. H. Jeong, Multi wall carbon nanotubes assisted synthesis of YVO₄:Eu³⁺ nanocomposites for display device applications, *Compos. B Eng.* 43 (2012) 1192–1195, <https://doi.org/10.1016/j.compositesb.2011.08.011>.
- [76] Y. Wang, W. Qin, J. Zhang, C. Cao, S. Lü, X. Ren, Photoluminescence of colloidal YVO₄:Eu/SiO₂ core/shell nanocrystals, *Opt Commun.* 282 (2009) 1148–1153, <https://doi.org/10.1016/j.optcom.2008.12.007>.
- [77] Y. Liang, J. Ouyang, H.W. Wang, P. Chui, K. Sun, Synthesis and characterization of core-shell structured SiO₂@YVO₄:Yb³⁺, Er³⁺ microspheres, *Appl. Surf. Sci.* 258 (2012) 3689–3694, <https://doi.org/10.1016/j.apsusc.2011.12.006>.
- [78] M. Shui, W. Zheng, J. Shu, Q. Wang, S. Gao, D. Xu, L. Chen, L. Feng, Y. Ren, Synthesis and electrochemical performance of Li_{1+x}V₃O₈ as cathode material prepared by citric acid and tartaric acid assisted sol-gel processes, *Curr. Appl. Phys.* 13 (2013) 517–521, <https://doi.org/10.1016/j.cap.2012.09.013>.
- [79] Z. Lin, S. Liu, X. Sun, M. Xie, J. Li, X. Li, Y. Chen, J. Chen, D. Huo, M. Zhang, Q. Zhu, M. Liu, The effects of citric acid on the synthesis and performance of silver-tin oxide electrical contact materials, *J. Alloys Compd.* 588 (2014) 30–35, <https://doi.org/10.1016/j.jallcom.2013.10.222>.
- [80] L. Alcaraz, Estudio de nanomateriales luminiscentes basados en matrices tipo zircón y nasicon, Doctoral Thesis, 2016. <https://eprints.ucm.es/id/eprint/42806/>.
- [81] R. Lisiecki, G. Dominiak-Dzik, T. Łukasiewicz, W. Ryba-Romanowski, Infrared-to-visible conversion of radiation in YVO₄ crystals doped with Yb³⁺ and Tm³⁺ ions, *J. Mol. Struct.* 704 (2004) 323–327, <https://doi.org/10.1016/j.molstruc.2004.01.062>.
- [82] Y.Z. Wang, D.C. Yu, H.H. Lin, Broadband three-photon near-infrared quantum cutting in Tm³⁺ singly doped YVO₄, *J. Appl. Phys.* 114 (2013), 203510, <https://doi.org/10.1063/1.4836897>.
- [83] D. Gao, Y. Liang, J. Gao, H. Xin, L. Wang, S. Yun, X. Zhang, Simultaneous luminescence enhancement and lifetime tuning of deep UV-NIR upconversion through controlling dopant concentration, *J. Lumin.* 238 (2021), 118261, <https://doi.org/10.1016/j.jlumin.2021.118261>.
- [84] T. Fu, X. Wang, H. Ye, Y. Li, X. Yao, Up-conversion luminescence and temperature sensing properties of CaBi₄Ti₄O₁₅:Tm³⁺, Yb³⁺ ceramics, *J. Electron. Mater.* 49 (2020) 5047–5052, <https://doi.org/10.1007/s11664-020-08239-y>.
- [85] D. Jaque, F. Vetrone, Luminescence nanothermometry, *Nanoscale* 4 (2012) 4301–4326, <https://doi.org/10.1039/C2NR30764B>.